

The geometric phase transition of the three-dimensional \mathbb{Z}_2 lattice gauge model

Ramgopal Agrawal,¹ Leticia F. Cugliandolo,¹ Lara Faoro,² Lev B. Ioffe,² and Marco Picco¹

¹Sorbonne Université, Laboratoire de Physique Théorique et Hautes Energies,

CNRS UMR 7589, 4 Place Jussieu, 75252 Paris Cedex 05, France

³Google Research, Mountain View, California 94043, USA

(Dated: September 24, 2024)

With intensive Monte Carlo simulations and finite size scaling we undertake a percolation analysis of Wegner’s three-dimensional \mathbb{Z}_2 lattice gauge model in equilibrium. We confirm that the loops threading excited plaquettes percolate at the thermal critical point T_c and we show that their critical exponents coincide with the ones of the loop representation of the dual 3D Ising model. We then construct Fortuin-Kasteleyn (FK) clusters using a random-cluster representation and find that they also percolate at T_c and moreover give access to all thermal critical exponents. The Binder cumulants of the percolation order parameter of both loops and FK clusters demonstrate a *pseudo first order* transition. This study sheds light on the critical properties of quantum error correction and lattice gauge theories.

Keywords: Toric codes, lattice gauge theories, critical phenomena, percolation

Lattice gauge theories were proposed by Wilson in 1974 [1] as a simplification of gauge field theories, in which the Euclidean spacetime is discretized on a lattice while preserving the local gauge invariance. The gauge fields represented by a dynamical variable are placed on the links of the lattice, whereas the matter fields are located on its sites. This allowed for the exploration of, e.g., QCD and Yang-Mills models using Monte Carlo sampling methods [2] and intriguing applications to condensed matter theory [3].

Notably, already in 1971 before Wilson’s proposal, Wegner [4] had introduced a gauge invariant version of the classical Ising model. This model is a formulation of a pure gauge lattice theory (no matter fields) with the gauge degrees of freedom being the elements of the \mathbb{Z}_2 group. With this model Wegner demonstrated the possibility of their being phase transitions of topological nature with no local order parameter.

Pure gauge lattice models also play a significant role in quantum computation as they provide a framework for exploring quantum error correction and topological quantum computing. The most celebrated example is the Toric Code [5, 6], in which the recovery procedure of the error chains exhibits a geometric phase transition. Below a certain threshold value of the error rate the error chains can be mapped to homologically trivial cycles (error correctable phase) with the help of an optimal decoder. Above it they are rather mapped to homologically nontrivial cycles (error non-correctable phase). An accurate estimate of the error bound in this code is obtained via a mapping to the *order-disorder* transition of classical disordered spin models on the Nishimori line [7, 8]. For the Toric Code with only qubit (flip/phase) errors, the corresponding model is the $2D \pm J$ Ising Model (IM) [7, 9]. When more *realistic* errors are included, i.e., measurement/read out errors [7, 10], the 3D \mathbb{Z}_2 lattice gauge model [7, 11–13] with quenched randomness is found. These connections have driven renewed interest in the phase transition problems of both

classical [13–15] and quantum lattice gauge models [16–19].

This being said, the identification and characterization of a phase transition between topological phases of a gauge system is still challenging. In the absence of a local order parameter, authors have largely relied [12–14, 20] on the behavior of the specific heat or global order parameters like Wilson [1, 21] and Polyakov loops [22, 23]. However, neither of them provides a complete description of criticality.

A natural route to follow would be to identify the objects that, with their fractal and statistical properties, characterize the phase transition completely. A plethora of works have analyzed different (geometrically defined) objects in a wide range of 3D systems. Some examples are cosmic strings in the early universe [24, 25], lines of darkness in light field [26], vortex loops in XY system [27, 28], complex $|\psi|^4$ theories [29–31], etc. Although these objects exhibit a unique geometric phase transition, their percolation threshold and critical properties do not always agree with the ones of the thermodynamic transition [32]. For instance, the domains formed by parallel nearest neighboring spins in the 3DIM do not percolate at the thermodynamic critical temperature T_c . Instead, the clusters constructed using the random-cluster representation [33], known as the *Fortuin-Kasteleyn* (FK) clusters, do percolate at T_c [34–36] and their critical exponents agree with the thermal critical ones.

In this Letter we study the celebrated 3D Wegner plaquette model from a geometric perspective. On the one hand, we analyze the geometric loops, constructed by joining the segments that thread the frustrated plaquettes. On the other hand, we introduce a FK formulation which involves larger graphs and we also investigate them in detail. With this study we unveil a full description of the thermal critical properties in which both kinds of objects play a relevant role.

Model and analysis. Wegner’s 3D \mathbb{Z}_2 gauge model is

defined by the Hamiltonian

$$H = -J \sum_{\mathbf{P}} U_{\mathbf{P}} = -J \sum_{\mathbf{P}} \prod_{\ell \in P} S_{\ell}, \quad (1)$$

where $S_{\ell} (= \pm 1)$ are Ising spins placed on the links, ℓ , of the square plaquettes, P , of the cubic lattice, and $J > 0$ is a coupling constant. The contribution from each plaquette, $U_{\mathbf{P}} = \prod_{\ell \in P} S_{\ell}$, takes either $+1$ (simple plaquette) or -1 (frustrated plaquette) values. Clearly, in any ground state $U_{\mathbf{P}} = +1 \forall \mathbf{P}$. Two fully magnetized ground states are $s_{\ell} = +1 \forall \ell$ or $s_{\ell} = -1 \forall \ell$. A local gauge transformation which consists in the simultaneous reversal of the 6 spins connected to a vertex leaves the Hamiltonian invariant. Thus, all the configurations generated by such local changes applied to any ground state are also ground states. This leads to an enormous degeneracy and a macroscopic ground state entropy [21].

The equilibrium magnetization density of the model (1) vanishes at all $T/J > 0$ [37]. Some understanding of the phase transition was gained by setting up a Kramers–Wannier duality [4]. In $D = 3$ the \mathbb{Z}_2 gauge model is dual to the 3D ferromagnetic IM. The critical inverse-temperature of the gauge model β_c is related to the one of the conventional IM β_c^* through $\beta_c J = -(\ln \tanh(\beta_c^* J^*))/2$. This yields $T_c \simeq 1.313346 J/k_B$ with k_B the Boltzmann constant. The static critical exponents are the same [4, 21, 38] as those in the dual model. Since there is no local order parameter in the gauge model, non-local gauge invariant ones have been used to characterize the two phases across the transition point — a low-temperature *deconfined* phase and a high temperature *confined* phase; see Supplemental Material (SM) for details.

After defining the two kinds of geometric objects that we will focus on, we apply a detailed finite size scaling analysis as in usual percolation studies [39–43]. With it:

- (i) We identify T_p and $1/\nu$ from the fraction of configurations having at least one spanning object, the spanning probability, P_S , and the Binder cumulant, U_4 , of the mass fraction m of the largest geometrical object.
- (ii) We obtain β/ν from the average mass fraction contributed by the largest object, or percolation strength, P , which acts as an order parameter.
- (iii) We deduce γ/ν from the susceptibility χ defined in terms of the fluctuations in m .
- (iv) We check the consistency of the analysis with measurements of the probability distribution of cluster sizes, which gives access to the Fisher exponent, τ , and the interfacial tension exponent σ , and the mass-radius of gyration relation which yields the fractal dimension, D_f .

The precise definition of all these geometric observables are recalled in SM.

Geometric line loops. The plaquettes with $U_{\mathbf{P}} = -1$ are excitations on top of the ground state which are gen-

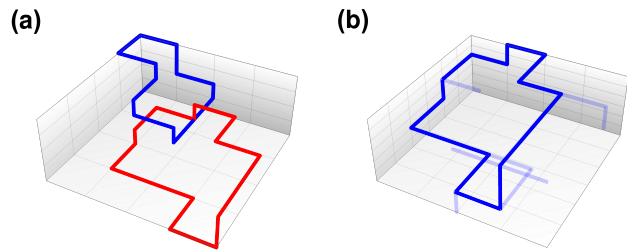


FIG. 1. Schematic representation of (a) line loops and (b) Fortuin-Kasteleyn (FK) graphs in the 3D gauge model. Different colors in (a) denote different loops. The line loop (in solid) and loops/dangling ends (in light) in (b) correspond to the lines threading frustrated and unfrustrated plaquettes, respectively. The latter are added to the solid loop with the probabilistic procedure explained in the text.

erated by thermal fluctuations. In a convenient dual representation each frustrated plaquette is threaded by a perpendicular segment with lattice spacing length. Since each link is shared by two faces of the cubes, only an even number of plaquettes on the faces of an elementary cube can have $U_{\mathbf{P}} = -1$. This can be seen as a consequence of the discretized version of Gauss’ law which implies conservation of electric flux in the absence of sources. These segments are then joined to form closed line loops or flux tubes; see the schematic Fig. 1(a). At low temperatures the loops are short while at higher temperatures, due to stronger thermal agitation, much longer and even giant system-sized loops can be formed. Naturally, a transition between a phase with finite size loops and another with a spanning one can be expected [44] and this underlines the need of a careful percolation analysis of these objects. As we explain in the SM, these loops can be treated as the graphs contributing to the low-temperature (LT) expansion of the partition function, and thanks to duality, they are akin to the high-temperature (HT) expansion graphs in the 3DIM.

Before going ahead with the analysis, it is worth discussing a technical aspect of it. The identification of the different closed loops in a given configuration remains an ambiguous task as the loops, especially those which are long, can have knots/branches, as shown in Fig. 1(a). These arise in the individual cubic cells when more than two plaquettes, that is four or with much lower probability six, are frustrated. In the literature, two methods are proposed [28–30] to resolve the knots. One is the “maximal reconnection method” in which the connections at a branching point is chosen so as to maximize the net length of the concerned loop; also see [45]. The other one is the “stochastic method” in which a dice is used to stochastically determine the connections. In our system, both methods give equivalent results [46]. Here we show data for the maximal reconnection rule only. In the SM we complement the analysis with data built with the stochastic rule. Further technical details of the Monte Carlo (MC) simulations [47] and the properties of other

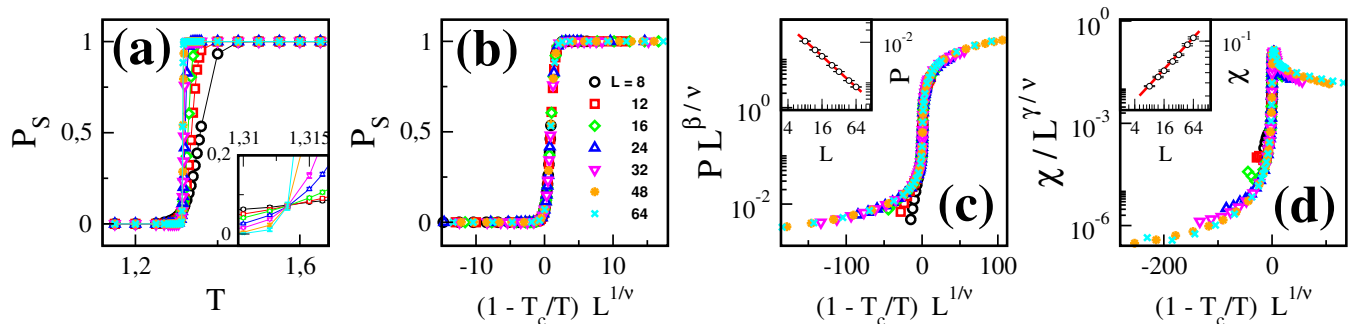


FIG. 2. **Geometric line loops.** (a) Spanning probability P_S vs temperature T . (b) P_S against the scaling variable $(1 - T_c/T)L^{1/\nu}$. (c) Rescaled plot of the percolation strength, $PL^{\beta/\nu}$ vs $(1 - T_c/T)L^{1/\nu}$. (d) Scaling plot of the susceptibility, $\chi/L^{\gamma/\nu}$ vs $(1 - T_c/T)L^{1/\nu}$. Different datasets represent systems of different linear size L , see the key in (b). The inset in (a) magnifies the intersection region in the main frame. The insets in (c) and (d) display the values of P and χ at the critical temperature T_c against the system size L , with solid lines representing the laws $P \sim L^{-\beta/\nu}$ and $\chi \sim L^{\gamma/\nu}$, respectively. For plots in (b)-(d), different parameters are fixed to $T_c = 1.3133$, $1/\nu = 1.58$, $\beta/\nu = 1.26$, and $\gamma/\nu = 0.47$. The collapses remain valid for the numerical estimates of parameters within error bars; see Table I.

observables of interest are also relegated to the SM.

Figure 2 presents the analysis of the geometric line loops constructed with the maximal connectivity rule. In (a) we plot the spanning probability P_S as a function of temperature for different system sizes L . For low T , P_S goes to zero, while for high T it approaches unity. At the percolation temperature T_p , $\lim_{L \rightarrow \infty} P_S$ approaches a universal value [48–50]. The value $T_p \simeq 1.3134(3)$ is thus obtained from the intersection point of the datasets for different L (see the inset). This value matches quite well the theoretical critical temperature T_c . A similar agreement is obtained for the loops with stochastic rule; see the SM. For a more stringent check, P_S is plotted against the scaling variable $(1 - T_c/T)L^{1/\nu}$ in Fig. 2(b). While fixing $T_p = T_c$ as obtained in panel (a) and treating the expo-

nent ν as a free variable, an excellent scaling collapse [51] is observed for $1/\nu \simeq 1.59(3)$, confirming a good match with the 3D Ising universality class ($1/\nu \sim 1.59$) [52–55]. We have also analyzed the Binder cumulant, U_4 , of the mass fraction m of largest geometrical object. This quantity also confirms the above obtained values of T_p and $1/\nu$; see the SM, and discussion below.

Panel (c) in Fig. 2 displays the scaling plot of the percolation probability P , which plays the role of an order parameter in percolation transitions. The value of the ratio β/ν was extracted from the decay of P as $L^{-\beta/\nu}$, at the temperature that we identified as the critical one with the analysis in (a)-(b). The excellent data collapse in the main panel, obtained with this value of β/ν , confirms the coherence of the procedure. Finally, in (d) we perform a similar analysis of the susceptibility χ : we extracted γ/ν from $\chi \sim L^{\gamma/\nu}$ at T_c and we checked consistency with the scaling analysis of the main panel. The fractal dimension D_f is also calculated from the average mass of the largest object $\langle s_l \rangle$ (Notice that $\langle s_l \rangle \sim L^{D_f}$ at T_c , as $\langle s_l \rangle \propto L^D P$; see the SM). The values of T_p , $1/\nu$, β/ν , γ/ν and D_f thus measured are reported in Table I. Interestingly, these values correspond to those of the HT graphs in the 3DIM within numerical precision [56–58]. We remark that for the loop representation the exponent $1/\nu$ coincides with the scaling dimension Δ_ϵ of the energy operator ϵ in the 3D $\mathcal{O}(N)$ singlet sector, while the other exponents β/ν and γ/ν are related to the scaling dimension Δ_T of a *nontrivial* symmetric tensor operator φ_{ab} which exists only in the 3D $\mathcal{O}(N)$ tensor sector [57, 58]; also see the SM.

The number density of loops with mass s , defined as the number of loops divided by the volume of the sample, is displayed in Fig. 3 on a double logarithmic scale. The algebraic decay $N(s)/L^3 \sim s^{-\tau}$ is evident from the plot, with a fit yielding the Fisher exponent $\tau \simeq 2.71(1)$. Using the relation $\tau = 1 + D/D_f$, we obtain $D_f = 1.74(1)$, which is also consistent with the value measured from

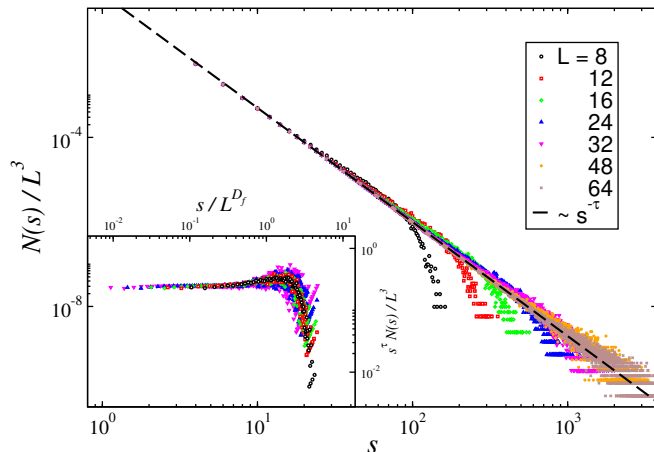


FIG. 3. **Geometric line loops.** Number density $N(s)/L^3$ vs mass s for different system sizes L (see the key) at the critical temperature T_c . The dashed line represents the law $s^{-\tau}$, with $\tau = 2.71$. The inset plots the scaling variable $s^\tau N(s)/L^3$ against s/L^{D_f} for data in the main frame, wherein τ and D_f are fixed to $\tau = 2.71$ and $D_f = 1.74$.

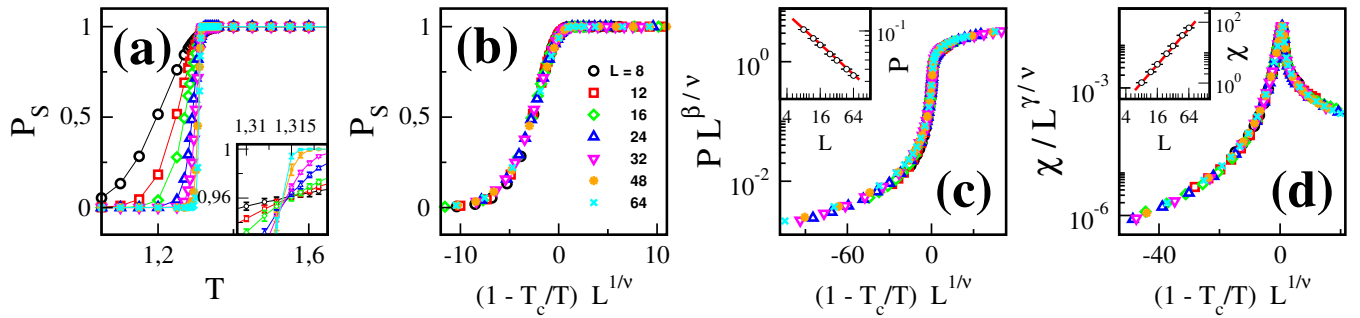


FIG. 4. **Fortuin-Kasteleyn graphs.** Various panels show plots similar to the ones in Fig. 2. For plots in (b)-(d), the parameters are fixed to $T_c = 1.3133$, $1/\nu = 1.58$, $\beta/\nu = 0.52$, and $\gamma/\nu = 1.97$. The collapses remain valid for the numerical estimates of parameters within error bars; see Table I.

$\langle s_l \rangle$, though it has large error bars. The inset shows a scaling plot, in good agreement with the estimates of τ and D_f from the main plot.

We remark that within numerical accuracy the relations $\beta/\nu = D - D_f$ and $\gamma/\nu = 2D_f - D$ are also obeyed, providing an independent check for our estimates. In conclusion, the line loops are equivalent to the HT expansion graphs of the 3DIM.

Fortuin-Kasteleyn (FK) graphs. Likewise the Ising model, we construct the FK clusters in the model system (1) by using the random cluster representation [59]. Herein, a bimodal random variable ($n_P = 0, 1$) is assigned to each plaquette on the lattice such that a plaquette is occupied if $n_P = 1$ and it is empty if $n_P = 0$; see the SM for details. The partition function $\mathcal{Z} = \sum_{\text{config.}} \prod_P e^{\beta J U_P}$ is given by

$$\mathcal{Z} = \sum_{\text{config.}} \prod_P \sum_{n_P=0,1} e^{\beta J [(1-q)\delta_{n_P,0} + q\delta_{U_P,1}\delta_{n_P,1}]}, \quad (2)$$

where $q \equiv 1 - e^{-2\beta J}$. A plaquette with $U_P = -1$ is always empty in this representation, while the one with $U_P = 1$ is empty with a probability $(1 - q)$. Therefore, a FK

cluster is formed by that set of empty plaquettes which are connected to each other, i.e., two neighboring ones belong to the same cube. The linear structures threading the FK clusters will have a closed loop form with attached linear protrusions; see the Schematic Fig. 1(b). These graphs will be typically larger than the geometric loops and are not completely closed.

In Fig. 4 we apply the percolation analysis on the FK graphs. The quality of the finite size scaling is also very satisfactory here. The values of T_p and $1/\nu$ obtained are, within numerical accuracy, the same as the ones derived for the geometric loops. The values of β/ν and γ/ν given in the Table I are, however, very different from the ones for the geometric loops and now indistinguishable from those of FK clusters in the 3DIM. This is because these FK exponents in the gauge model are related to the scaling dimension Δ_σ of the *singlet* spin operator σ of the 3DIM [57].

The analysis of the number density of the mass of the FK graphs and their fractal properties, similar to the one presented in Fig. 3 for the geometric loops, yields the value of D_f reported in Table I. It also satisfies the critical scaling relations; see the SM.

Let us finally discuss the nature of the geometric transition. We have seen from the critical scaling analysis that the percolation transition in both geometric loops and FK clusters is continuous. However, the Binder cumulant U_4 of $m = s_l/(3L^3)$ has a peculiar behavior. For both the geometric line loops and FK graphs, right below T_c , a dip is observed in U_4 , see Fig. 5(a) for the FK case, which does not vary much with system size (contrary to what would happen in a first order phase transition [60]). Moreover, the data satisfy the finite size scaling $U_4 = f_U[(1 - T_c/T)L^{1/\nu}]$, as shown in Fig. 5(b). This behavior is identified as a *pseudo first order transition* in the literature [61, 62]. It arises from anomalies in the order parameter distribution $P_{\text{dist}}(m)$ below the critical temperature; see the SM.

Conclusion. We studied the geometrical properties of the closed loops formed by the connected segments which thread the frustrated plaquettes. We confirmed that they percolate at T_c , as found in Ref. [44]. With finite size

System	T_c or T_p	$1/\nu$	β/ν	γ/ν	D_f
FK IM[52–55]	1.3133	1.587	0.518	1.964	2.482
HT IM[56–58]	–	1.587	1.265	0.470	1.735
Loops GM	1.3134(3)	1.592(28)	1.261(8)	0.486(18)	1.738(8)
FK GM	1.3137(4)	1.581(18)	0.519(5)	1.971(7)	2.481(6)

TABLE I. Comparison between the FK clusters in the 3DIM (FK IM, first row), high temperature expansion graphs in the 3DIM (HT IM, second row), geometric loops in the 3D gauge model (Loops GM, third row) and FK clusters of the 3D gauge model (FK GM, fourth row). Estimates of the critical temperature T_c ($\equiv 1/\beta_c$) (3DGM), and percolation temperature T_p for geometrical objects, critical exponents $1/\nu$, β/ν , γ/ν , and fractal dimension D_f , see the main text for details. Note that for the HT values only $1/\nu$ and β/ν were computed in literature, while $\gamma/\nu = D - 2\beta/\nu$ and $D_f = D - \beta/\nu$ were used to calculate the values in the table.

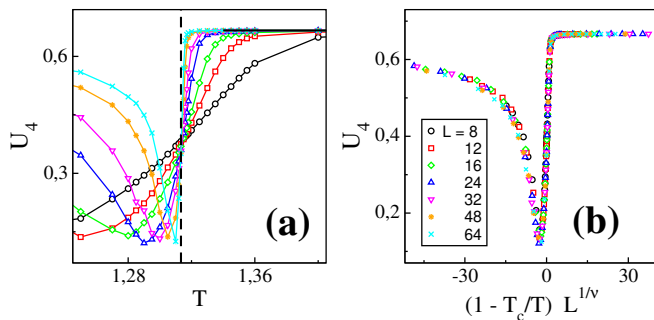


FIG. 5. Binder cumulant U_4 of the mass fraction $m = s_1/(3L^3)$ of the largest FK cluster. (a) Zoom around the critical temperature T_c , signaled with a vertical dashed line. The horizontal solid line represents the large- T behavior, $U_4 = 2/3$. (b) Scaling of the data fixing $T_p = T_c$ and $1/\nu = 1.58$. Different datasets correspond to different systems of linear size L given in the key.

scaling of percolation observables we obtained the critical exponents, which are in excellent agreement with the ones of the HT graphs of the dual 3DIM. Next, we identified the FK graphs using the random cluster representation and we showed that they also percolate at T_c and their critical exponents are the thermal ones of the dual 3DIM. Moreover, the non-Gaussian behavior of the order parameter distribution for both loops and FK clusters departs from the one of conventional second order phase

transitions and is the one of a pseudo first order one.

One immediate consequence of our result concerns cluster MC algorithms. An early proposal [63] to exploit FK graphs to accelerate MC simulations was ignored since questions about the validity of detailed balance and the relevance to characterize the critical point with these objects remained unanswered. Our analysis lifts these doubts and shows that these graphs can be used in MC algorithms to beat critical slowing down.

The present analysis should also be useful to understand the phase transitions in lattice gauge theories and topological codes. In recent work [13, 14] a first order transition was claimed in the gauge theory with randomness, using the skewness of the smallest Wilson loop distribution as an indicator. Since the thermodynamic transition in the disorder-free case is continuous, and given the well-known fact that disorder tends to soften the phase transitions (making first order ones continuous) [64], we think that a discontinuous transition in the disorder case is unlikely. The percolation analysis can provide a quantitative resolution of this issue.

ACKNOWLEDGMENTS

The authors acknowledge financial support from the French grant ANR-19-CE30-0014 and a Google Gift. The simulations were performed on the SACADO MeSU platform at Sorbonne Université. RA thanks E. Trevisani and K. J. Wiese for useful discussions.

-
- [1] K. G. Wilson, Confinement of quarks, *Phys. Rev. D* **10**, 2445 (1974).
- [2] J. B. Kogut, The lattice gauge theory approach to quantum chromodynamics, *Rev. Mod. Phys.* **55**, 775 (1983).
- [3] E. Fradkin, *Quantum Field Theory: An Integrated Approach* (Princeton University Press, 2021).
- [4] F. J. Wegner, Duality in Generalized Ising Models and Phase Transitions without Local Order Parameters, *J. Math. Phys.* **12**, 2259 (1971).
- [5] A. Y. Kitaev, Quantum computations: algorithms and error correction, *Russ. Math. Surv.* **52**, 1191 (1997).
- [6] A. Kitaev, Fault-tolerant quantum computation by anyons, *Ann. Phys.* **303**, 2 (2003).
- [7] E. Dennis, A. Kitaev, A. Landahl, and J. Preskill, Topological quantum memory, *J. Math. Phys.* **43**, 4452 (2002).
- [8] H. Nishimori, *Statistical physics of spin glasses and information processing: an introduction* (Clarendon Press, Oxford, 2001).
- [9] R. Agrawal, L. F. Cugliandolo, L. Faoro, L. B. Ioffe, and M. Picco, Nonequilibrium critical dynamics of the two-dimensional $\pm j$ Ising model, *Phys. Rev. E* **108**, 064131 (2023); Dynamical critical behavior on the nishimori point of frustrated ising models, *Phys. Rev. E* **110**, 034120 (2024).
- [10] A. G. Fowler, M. Mariantoni, J. M. Martinis, and A. N. Cleland, Surface codes: Towards practical large-scale quantum computation, *Phys. Rev. A* **86**, 032324 (2012).
- [11] C. Wang, J. Harrington, and J. Preskill, Confinement-higgs transition in a disordered gauge theory and the accuracy threshold for quantum memory, *Ann. Phys.* **303**, 31 (2003).
- [12] T. Ohno, G. Arakawa, I. Ichinose, and T. Matsui, Phase structure of the random-plaquette z_2 gauge model: accuracy threshold for a toric quantum memory, *Nucl. Phys. B* **697**, 462 (2004).
- [13] R. S. Andrist, H. G. Katzgraber, H. Bombin, and M. A. Martin-Delgado, Tricolored lattice gauge theory with randomness: fault tolerance in topological color codes, *New J. Phys.* **13**, 083006 (2011).
- [14] R. S. Andrist, H. G. Katzgraber, H. Bombin, and M. A. Martin-Delgado, Error tolerance of topological codes with independent bit-flip and measurement errors, *Phys. Rev. A* **94**, 012318 (2016).
- [15] R. S. Andrist, H. Bombin, H. G. Katzgraber, and M. A. Martin-Delgado, Optimal error correction in topological subsystem codes, *Phys. Rev. A* **85**, 050302 (2012).
- [16] C. Castelnuovo and C. Chamon, Topological order in a three-dimensional toric code at finite temperature, *Phys. Rev. B* **78**, 155120 (2008).
- [17] G. Mazzola, S. V. Mathis, G. Mazzola, and I. Tavernelli, Gauge-invariant quantum circuits for $u(1)$ and Yang-Mills lattice gauge theories, *Phys. Rev. Res.* **3**, 043209 (2021).

- (2021).
- [18] G. Zhu, T. Jochym-O'Connor, and A. Dua, Topological order, quantum codes, and quantum computation on fractal geometries, *PRX Quantum* **3**, 030338 (2022).
- [19] A. Apte, A. Ashmore, C. Cordova, and T.-C. Huang, *Deep learning lattice gauge theories* (2024), [arXiv:2405.14830 \[hep-lat\]](https://arxiv.org/abs/2405.14830).
- [20] N. Xu, C. Castelnovo, R. G. Melko, C. Chamon, and A. W. Sandvik, Dynamic scaling of topological ordering in classical systems, *Phys. Rev. B* **97**, 024432 (2018).
- [21] J. B. Kogut, An introduction to lattice gauge theory and spin systems, *Rev. Mod. Phys.* **51**, 659 (1979).
- [22] A. Polyakov, Compact gauge fields and the infrared catastrophe, *Phys. Lett. B* **59**, 82 (1975).
- [23] B. Svetitsky and L. G. Yaffe, Critical behavior at finite-temperature confinement transitions, *Nucl. Phys. B* **210**, 423 (1982).
- [24] T. W. B. Kibble, Topology of cosmic domains and strings, *J. Phys. A: Math. Gen.* **9**, 1387 (1976).
- [25] T. Vachaspati and A. Vilenkin, Formation and evolution of cosmic strings, *Phys. Rev. D* **30**, 2036 (1984).
- [26] K. O'Holleran, M. R. Dennis, F. Flossmann, and M. J. Padgett, Fractality of light's darkness, *Phys. Rev. Lett.* **100**, 053902 (2008).
- [27] G. Kohring, R. E. Shrock, and P. Wills, Role of vortex strings in the three-dimensional $o(2)$ model, *Phys. Rev. Lett.* **57**, 1358 (1986).
- [28] K. Kajantie, M. Laine, T. Neuhaus, A. Rajantie, and K. Rummukainen, $O(2)$ symmetry breaking versus vortex loop percolation, *Phys. Lett. B* **482**, 114 (2000).
- [29] E. Bittner, A. Krinner, and W. Janke, Vortex-line percolation in the three-dimensional complex $|\psi|^4$ model, *Phys. Rev. B* **72**, 094511 (2005).
- [30] M. Kobayashi and L. F. Cugliandolo, Quench dynamics of the three-dimensional $U(1)$ complex field theory: Geometric and scaling characterizations of the vortex tangle, *Phys. Rev. E* **94**, 062146 (2016).
- [31] M. Kobayashi and L. F. Cugliandolo, Thermal quenches in the stochastic Gross-Pitaevskii equation: Morphology of the vortex network, *Europhys. Lett.* **115**, 20007 (2016).
- [32] H. Müller-Krumbhaar, Percolation in a lattice system with particle interaction, *Phys. Lett. A* **50**, 27 (1974).
- [33] C. Fortuin and P. Kasteleyn, On the random-cluster model: I. Introduction and relation to other models, *Physica* **57**, 536 (1972).
- [34] A. Coniglio and W. Klein, Clusters and Ising critical droplets: a renormalisation group approach, *J. Phys. A: Math. Gen.* **13**, 2775 (1980).
- [35] V. S. Dotsenko, M. Picco, P. Windey, G. Harris, E. Martinec, and E. Marinari, Self-avoiding surfaces in the 3D Ising model, *Nucl. Phys. B* **448**, 577 (1995).
- [36] P. Hou, S. Fang, J. Wang, H. Hu, and Y. Deng, Geometric properties of the Fortuin-Kasteleyn representation of the Ising model, *Phys. Rev. E* **99**, 042150 (2019).
- [37] In fact, Elitzur's theorem states that only the quantities which are gauge invariant remain nonzero.
- [38] E. Kehl, H. Satz, and B. Wlzl, Critical exponents of Z_2 gauge theory in $(3 + 1)$ dimensions, *Nucl. Phys. B* **305**, 324 (1988).
- [39] D. Stauffer and A. Aharony, *Introduction to percolation theory* (CRC press, 2018).
- [40] J. W. Essam, Percolation theory, *Rep. Prog. Phys.* **43**, 833 (1980).
- [41] H. J. Herrmann and H. E. Stanley, Building blocks of percolation clusters: Volatile fractals, *Phys. Rev. Lett.* **53**, 1121 (1984).
- [42] A. A. Saberi, Recent advances in percolation theory and its applications, *Phys. Rep.* **578**, 1 (2015).
- [43] Y. M. Strelniker, S. Havlin, and A. Bunde, Fractals and percolation, in *Encyclopedia of Complexity and Systems Science*, edited by R. A. Meyers (Springer New York, New York, NY, 2009) pp. 3847–3858.
- [44] M. B. Hastings, G. H. Watson, and R. G. Melko, Self-correcting quantum memories beyond the percolation threshold, *Phys. Rev. Lett.* **112**, 070501 (2014).
- [45] In the present system, such a loop is formed by a set of neighboring frustrated plaquettes. The plaquettes belonging to the same cubic cell on a lattice are the neighboring plaquettes.
- [46] In the stochastic method the loops are relatively smaller than those obtained from the maximal reconnection method. Since there are less number of knots/branches at $T \leq T_c$, the statistics of the loops obtained from different methods remains the same at such temperatures. However, at higher temperatures $T > T_c$, they show significant differences; see the SM and Refs. [65].
- [47] M. Newman and G. Barkema, *Monte Carlo Methods in Statistical Physics* (Oxford University Press, New York, 1999).
- [48] R. P. Langlands, C. Pichet, P. Pouliot, and Y. Saint-Aubin, On the universality of crossing probabilities in two-dimensional percolation, *J. Stat. Phys.* **67**, 553 (1992).
- [49] R. M. Ziff, Spanning probability in 2d percolation, *Phys. Rev. Lett.* **69**, 2670 (1992).
- [50] J.-P. Hovi and A. Aharony, Scaling and universality in the spanning probability for percolation, *Phys. Rev. E* **53**, 235 (1996).
- [51] To quantify the nature of scaling collapses, we have extracted a local-linearity function (analogous to *reduced* χ^2) from the participating data points. It serves as a measure for the goodness of the collapse. See N. Kawashima and N. Ito, Critical behavior of the three-dimensional $\pm j$ model in a magnetic field, *J. Phys. Soc. Jpn.* **62**, 435 (1993).
- [52] M. Hasenbusch, Finite size scaling study of lattice models in the three-dimensional Ising universality class, *Phys. Rev. B* **82**, 174433 (2010).
- [53] F. Kos, D. Poland, D. Simmons-Duffin, and A. Vichi, Precision islands in the Ising and $O(N)$ models, *J. High Energy Phys.* **2016** (8), 1.
- [54] D. Simmons-Duffin, The lightcone bootstrap and the spectrum of the 3d Ising CFT, *J. High Energy Phys.* **2017** (3), 1.
- [55] A. M. Ferrenberg, J. Xu, and D. P. Landau, Pushing the limits of monte carlo simulations for the three-dimensional Ising model, *Phys. Rev. E* **97**, 043301 (2018).
- [56] F. Winter, W. Janke, and A. M. J. Schakel, Geometric properties of the three-dimensional Ising and XY models, *Phys. Rev. E* **77**, 061108 (2008).
- [57] H. Shimada and S. Hikami, Fractal dimensions of self-avoiding walks and Ising high-temperature graphs in 3d conformal bootstrap, *J. Stat. Phys.* **165**, 1006 (2016).
- [58] M. Kompaniets and K. J. Wiese, Fractal dimension of critical curves in the $O(n)$ -symmetric ϕ^4 model and crossover exponent at 6-loop order: Loop-erased random walks, self-avoiding walks, Ising, XY, and Heisenberg models, *Phys. Rev. E* **101**, 012104 (2020).

- [59] An implementation of cluster Monte Carlo algorithm in the gauge model using random cluster representation [33, 34] was earlier proposed in Ref. [63].
- [60] K. Binder, Critical properties from Monte Carlo coarse graining and renormalization, *Phys. Rev. Lett.* **47**, 693 (1981); K. Binder and D. P. Landau, Finite-size scaling at first-order phase transitions, *Phys. Rev. B* **30**, 1477 (1984).
- [61] S. Jin, A. Sen, and A. W. Sandvik, Ashkin-teller criticality and pseudo-first-order behavior in a frustrated Ising model on the square lattice, *Phys. Rev. Lett.* **108**, 045702 (2012).
- [62] Y. Q. Qin, Y.-Y. He, Y.-Z. You, Z.-Y. Lu, A. Sen, A. W. Sandvik, C. Xu, and Z. Y. Meng, Duality between the deconfined quantum-critical point and the bosonic topological transition, *Phys. Rev. X* **7**, 031052 (2017).
- [63] R. Ben-Av, D. Kandel, E. Katznelson, P. Lauwers, and S. Solomon, Critical acceleration of lattice gauge simulations, *J. Stat. Phys.* **58**, 125 (1990).
- [64] M. Aizenman and J. Wehr, Rounding of first-order phase transitions in systems with quenched disorder, *Phys. Rev. Lett.* **62**, 2503 (1989).
- [65] P.-G. De Gennes, *Scaling concepts in polymer physics* (Cornell University Press, 1979); L. D. C. Jaubert, M. Haque, and R. Moessner, Analysis of a fully packed loop model arising in a magnetic Coulomb phase, *Phys. Rev. Lett.* **107**, 177202 (2011); A. Nahum, J. T. Chalker, P. Serna, M. Ortuño, and A. M. Somoza, Length distributions in loop soups, *Phys. Rev. Lett.* **111**, 100601 (2013).

SUPPLEMENTAL MATERIAL

S1. TECHNICAL DETAILS AND METHODOLOGY

In this section, we present the methods used to simulate the model Hamiltonian (1) of the main text and some other technical details; see Fig. S1 for a schematic plot of the system defined on a simple cubic lattice.

We use Monte Carlo methods to generate the equilibrium spin configurations. With them we study the phase transition in the geometrical network formed by the lines threading the frustrated plaquettes. For this purpose, the initial system configuration at time $t = 0$ is prepared in a high temperature phase by assigning equally probable random values (± 1) to each link spin S_ℓ . Such a configuration belongs to the *confined* phase, where each plaquette term U_P of the Hamiltonian (1) takes a value $+1$ or -1 with probability a half. The system is then quenched to 39 different temperature values $T \in [0.8, 1.7]$, which lie above, below, and at the critical temperature $T = T_c$. We exploit the single spin flip Metropolis rule [47] to evolve the system at the different quench temperatures, with the transition rate

$$W(S_\ell \rightarrow -S_\ell) = \frac{1}{\mathcal{N}} \min \left\{ 1, e^{-\frac{\Delta E}{T}} \right\}, \quad (\text{S1})$$

where ΔE is the energy difference generated by the proposed spin flip, the Boltzmann constant k_B is set to unity hereafter, and $\mathcal{N} = 3L^3$ is the number of link spins in the system with L being its linear size. Notice that the flip of a single spin S_ℓ at link ℓ causes the flip of the sign of all four plaquettes sharing the common link ℓ . This ensures that gauge invariance is respected during the dynamics. Time is measured in terms of Monte Carlo Steps (MCS), each corresponding to \mathcal{N} attempted spin flips.

To ensure that the system evolved by the above rule (S1) reaches thermal equilibrium at the quench temperature T , we investigate the behavior of average internal energy as a function of time. We let each system of size L thermalize until $t \sim 1 \times 10^5$ MCS ($t \sim 5 \times 10^5$ MCS at low T) after a start from $t = 0$. We confirm that the average internal energy saturates to a temperature dependent but time independent value. In order to obtain several equilibrium configurations from a single Monte Carlo run, we further ensure that a configuration measured at time t has become completely decorrelated from a previous equilibrium configuration at time $t_0 < t$. This is done by calculating the spin-spin autocorrelation function $\overline{S_\ell(t_0)S_\ell(t)}$, whereby (\dots) represents a spatial average, i.e., an average over all the $3L^3$ link spins. This quantity decays from unity with increase in time t and finally attains a value around zero when a complete decorrelation from the initial state at t_0 has occurred.

Since our primary goal is to investigate the phase transition characteristics of the geometrical networks in an infinitely size system, we undertake a finite size scaling analysis using systems of linear sizes $L =$

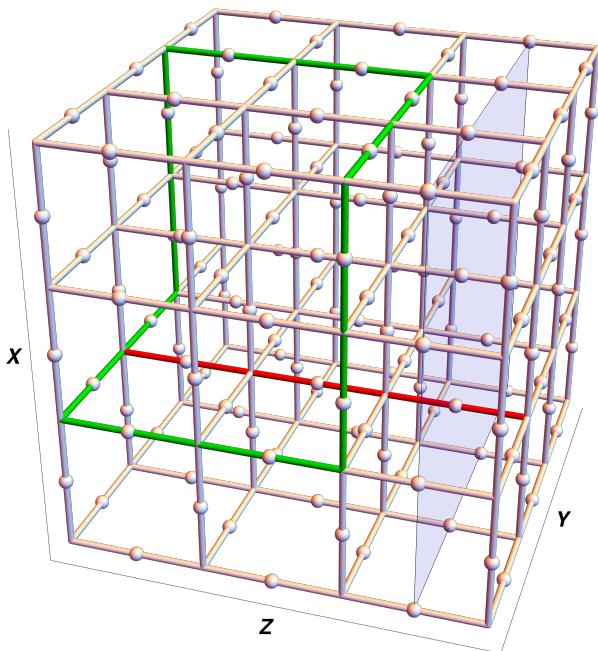


FIG. S1. 3D pure gauge model. A spin S_ℓ is placed at each link ℓ of the cubic lattice. In the figure it is denoted by a “sphere”. The contour represented in green (light) is a typical Wilson loop. The red (solid) line passing through the links in the periodic z -direction represents a Polyakov loop p ; see details in the text. Flipping all the spins lying on the gray (shaded) plane changes the sign of p . Such an operation is referred to as global \mathbb{Z}_2 center transformation.

8, 12, 16, 24, 32, 48, 64; with each system defined on a simple cubic lattice. The lattice spacing/constant is fixed to unity without the loss of any generality. Additionally, periodic boundary conditions (PBCs) are imposed in all the three spatial directions.

To gain good statistical accuracy, we average the observable quantities of interest (see section ahead) over a large number of equilibrium configurations for a fixed system size (100000 – 200000 for $L = 8 - 32$, and 50000 for $L = 48$ and $L = 64$). This complete study took over a half million of CPU hours.

S2. THERMODYNAMIC PHASE TRANSITION

This section summarizes the thermodynamic phase transition in the model system (1) of the main text.

This model shows a phase transition at the critical temperature $T_c \simeq 1.313346 J/k_B$, with the same thermal critical exponents [4, 21, 38] as the ones of the three dimensional (3D) Ising model. The magnetization remains zero at all temperatures; however, the average internal energy per spin $\langle E \rangle$ and its fluctuations (i.e., the specific heat C) exhibit critical behavior near T_c . Notice that in the model (1), $\langle E \rangle$ can be calculated from the average

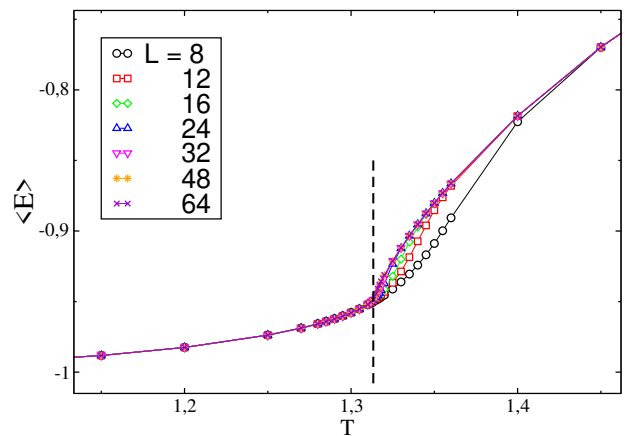


FIG. S2. Average energy per spin $\langle E \rangle$ vs temperature T for different system sizes (see the key). The dashed vertical line locates the critical temperature T_c [4, 21].

number of plaquettes $\langle \mathcal{N}_- \rangle$ with -1 value,

$$\langle E \rangle = J \left(2 \frac{\langle \mathcal{N}_- \rangle}{\mathcal{N}} - 1 \right), \quad (\text{S2})$$

where the symbol $\langle (\dots) \rangle$ represents the ensemble average, i.e., the average over independent equilibrium configurations. Remember that \mathcal{N} denotes the number of all plaquettes (both with values $+1$ and -1), which is also the same as the number of link spins for our cubic lattice system. In Fig. S2, $\langle E \rangle$ is plotted against T for different system sizes L . For increasing values of L , the variation of $\langle E \rangle$ with T becomes more and more pronounced near T_c , as expected. The specific heat can be calculated from the following relation

$$C = \frac{\langle E^2 \rangle - \langle E \rangle^2}{T^2}, \quad (\text{S3})$$

valid in equilibrium. It obeys the finite size scaling form,

$$C = L^{\alpha/\nu} F \left[\left(1 - \frac{T_c}{T} \right) L^{1/\nu} \right], \quad (\text{S4})$$

where α and ν are the standard thermal critical exponents. In Fig. S3(a), C is plotted against temperature T . For increasing values of L , the peak shifts towards the critical temperature T_c . The finite size scaling function (S4) is tested in Fig. S3(b), where we used the known critical exponents of the 3D IM; see the main text. Clearly, the scaling of datasets is not good at all. It was expected due to strong logarithmic corrections to the power law $C \propto |1 - T_c/T|^{-\alpha}$. Notice that the latter holds very close to T_c only; otherwise, $C \propto \log |1 - T_c/T| + \text{const.}$, e.g., see Ref. [30].

In the absence of a local order parameter, gauge invariant correlation functions are used as the global order parameters in model (1), e.g., Wilson loops [1, 21],

$$W(\mathbb{C}) = \prod_{\ell \in \mathbb{C}} S_\ell, \quad (\text{S5})$$

where \mathbb{C} is a contour of link spins. The ensemble average of $W(\mathbb{C})$ falls exponentially with the *minimal* area covered by the contour \mathbb{C} in the phase above (confinement) the critical temperature T_c , while it falls exponentially with the perimeter of \mathbb{C} in the phase below (deconfinement) T_c , as the loop becomes larger [21]. It indicates that this quantity is prone to strong finite size effects and not suitable to characterize different phases across T_c on a small sized system. A typical construction of a Wilson loop on the cubic lattice is shown in Fig. S1.

There is another related quantity, the so-called Polyakov loop p [22, 23], which is also interesting. It is simply the product of link spins lying on a line spanning across one fixed periodic boundary direction, say z (see Fig. S1). By construction, this quantity remains invariant under the local gauge transformation. However, it is not invariant under a global \mathbb{Z}_2 center symmetry [23]. The spatial average of p over the xy -plane, say \bar{p} , is zero at high temperatures, and $+1$ or -1 in the ground state at $T = 0$.

In Fig. S4, the ensemble averaged absolute value of the Polyakov loop $\langle |\bar{p}| \rangle$ is plotted against temperature T for different system sizes L . Notice that this quantity is not directly related to any finite size scaling arguments [38]; therefore, it is not suitable to calculate the critical exponents.

S3. GEOMETRIC OBSERVABLES

In this section, we detail different observable quantities used to study the geometrically defined objects that we use in the main text.

Let us first list all the observables before discussing their definitions and scaling properties.

- (1) The percolation strength P .
- (2) The susceptibility χ .
- (3) The Binder cumulant U_4 .
- (4) The spanning probability P_S .
- (5) The number density $N(s)$ of objects with mass s .
- (6) The average mass $\langle s_l \rangle$ of the largest object.
- (7) The average mass $\langle s \rangle$ of an object with radius of gyration R_g .

These are standard quantities used in the study of percolation problems [39, 40, 42, 43]. We have used the name “mass” to indicate the “size”, that is, the number of elements, in an object.

The percolation strength P is the average of the fluctuating mass fraction $m = s_l/(3L^3)$ contributed by the largest geometrical object in a configuration. For an infinite system, this quantity grows as $P \propto (T - T_p)^\beta$ above the percolation threshold T_p and it vanishes otherwise. That is why P plays the role of an order parameter in the percolation transition.

Another closely related quantity which can be fetched from the mass fraction m is the susceptibility χ . It is

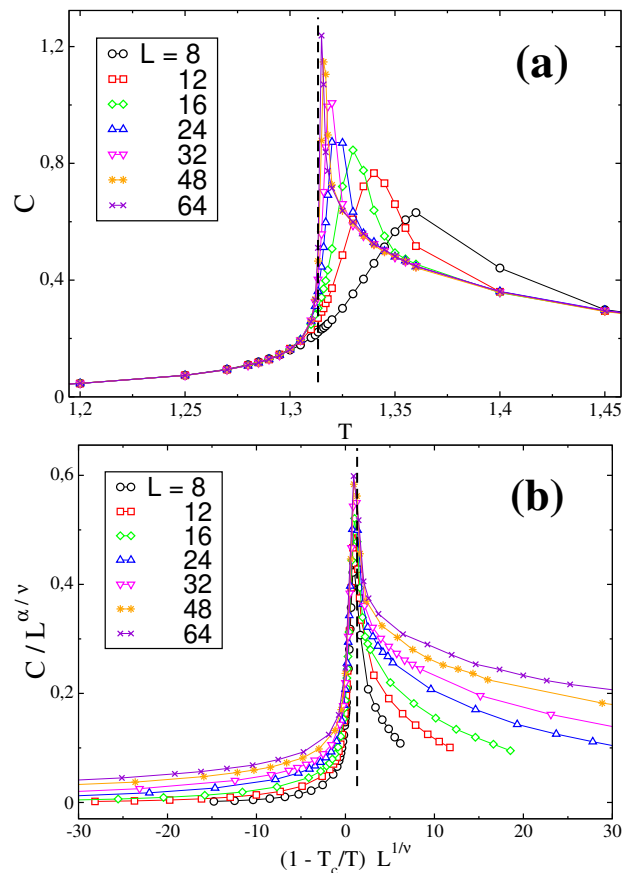


FIG. S3. (a) Specific heat C vs temperature T for different system sizes (see the key). (b) Scaling plot $C/L^{\alpha/\nu}$ vs $(1 - T_c/T)L^{1/\nu}$ for the raw data in (a). The dashed vertical line locates the critical temperature T_c . The lines joining different symbols are shown as a guide to eye.

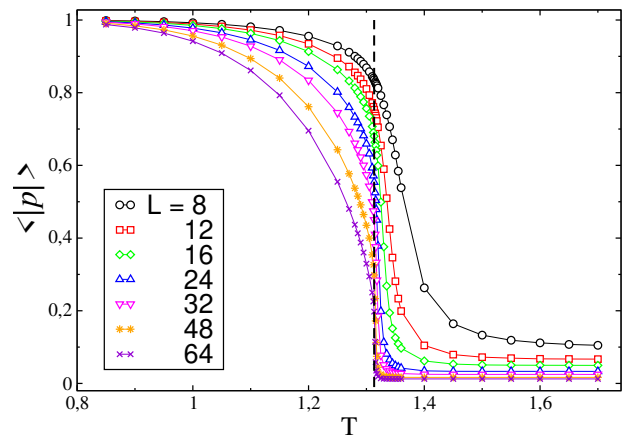


FIG. S4. Average Polyakov loop $\langle |\bar{p}| \rangle$ vs temperature T for different system sizes (see the key). The dashed vertical line is placed at the critical temperature T_c .

defined as,

$$\chi = \frac{L^D}{T} (\langle m^2 \rangle - \langle m \rangle^2), \quad (\text{S6})$$

where the symbol $\langle(\dots)\rangle$ denotes the average over independent equilibrium configurations. At T_p , it diverges algebraically as $\chi \propto |T - T_p|^{-\gamma}$.

These quantities obey the following finite size scaling forms,

$$P = L^{-\beta/\nu} f_P \left[\left(1 - \frac{T_p}{T}\right) L^{1/\nu} \right], \quad (\text{S7})$$

$$\chi = L^{\gamma/\nu} f_\chi \left[\left(1 - \frac{T_p}{T}\right) L^{1/\nu} \right], \quad (\text{S8})$$

where β , γ , and ν are the standard critical exponents. Likewise the thermal phase transitions, one can also calculate the Binder cumulant U_4 from the distribution of the mass fraction m of largest object as, $U_4 = 1 - \langle m^4 \rangle / 3 \langle m^2 \rangle^2$ (see Sec. S8 for details).

The spanning probability P_S is the fraction of configurations having at least one spanning object (loop/cluster). By spanning object we mean that it crosses/percolates the system in an arbitrary direction. Obviously, in an infinite system, it will be zero below T_p and unity above T_p . Therefore, its scaling form is

$$P_S = f_S \left[\left(1 - \frac{T_p}{T}\right) L^{1/\nu} \right] \quad (\text{S9})$$

with $\lim_{x \rightarrow \infty} f_S[x] = 1$ and $\lim_{x \rightarrow -\infty} f_S[x] = 0$. At $T = T_p$, P_S attains an L -independent *universal* value, $P_S = f_S[0]$. Due to this characteristic, P_S is useful to determine the location of T_p , whereby the datasets belonging to the different L should intersect each other; see the main text.

The quantity $N(s)$, the number density of loops/clusters with mass s normalized by volume L^3 , also reveal many interesting properties of thermodynamic as well as geometrical transitions [39, 40, 42, 43]. In the infinite size limit, below and close to T_p , $N(s)$ obeys the following form,

$$N(s)/L^3 \simeq s^{-\tau} e^{-s\epsilon}, \quad \epsilon \propto (T_p - T)^{1/\sigma}, \quad (\text{S10})$$

where τ is an exponent related to the interfacial fractal dimension D_f of the geometrical objects as,

$$\tau = 1 + D/D_f. \quad (\text{S11})$$

The parameter ϵ is the interfacial tension of the objects such that $\epsilon \rightarrow 0$ as $T \rightarrow T_p$, and the associated exponent is

$$\sigma = 1/(D_f \nu). \quad (\text{S12})$$

Finally, we discuss different methods to calculate the fractal dimension D_f of the geometrically defined objects. In an equilibrium configuration at any temperature T , the geometric objects are fractal at length scales smaller than the correlation length ξ . In particular, at T_p , ξ is comparable to the system size and, therefore, the average mass $\langle s_l \rangle$ of the largest object increases in a power law fashion with the system size [39, 42]

$$\langle s_l \rangle \sim L^{D_f}, \quad (\text{S13})$$

with D_f being the fractal dimension of the object. The notation $\langle(\dots)\rangle$ was defined above. Taking into account the fact that the average mass satisfies $\langle s_l \rangle \propto L^D P$, then

$$D_f = D - \beta/\nu. \quad (\text{S14})$$

Another well-known method to measure a fractal dimension is the box counting approach: plot the average mass $\langle s \rangle$ of an object against its linear extent or radius of gyration R_g . For fractal objects,

$$\langle s \rangle \sim R_g^{D_f}. \quad (\text{S15})$$

S4. LOW TEMPERATURE EXPANSION GRAPHS AND LINE LOOPS

In order to understand the percolation transition of closed line loops formed using the maximal or stochastic connection rules, we look at the low-temperature (LT) expansion of the partition function

$$\mathcal{Z} = \sum_{\text{config.}} e^{-\beta H} = \sum_{\text{config.}} \prod_P e^{K U_P}, \quad (\text{S16})$$

where $K = \beta J$. Substituting $U_P = 1 - 2W_P$, we get

$$\mathcal{Z} = e^{3NK} \sum_{\text{config.}} \prod_P e^{-2KW_P}. \quad (\text{S17})$$

Here, N is the number of sites in the system. From the above Eq. (S17), one can easily obtain the LT expansion, with e^{-2K} being the LT expansion parameter,

$$\mathcal{Z} = e^{3NK} 2^N [1 + 3N (e^{-2K})^4 + 18N (e^{-2K})^6 + \dots]. \quad (\text{S18})$$

In the above series, the terms with exponents 4 and 6 on the right hand side represent the loop excitations in the ground state, which are formed by the flip of one link-spin and two link-spins belonging to any plaquette, respectively. By flipping more spins in the ground state, higher loop excitations (higher terms of the above series) will be obtained. In this sense, the closed line loops formed by threading the neighboring frustrated plaquettes (see the main text) are the *LT expansion graphs* of the partition function (S18) in the loop representation; also see Sec. S5.

Now, as we know, the model Hamiltonian (1) of the main text is (Kramer-Wannier) dual to the 3D pure Ising model. This means that the high-temperature (HT) expansion of the Ising model is analogous to the LT expansion of the gauge model obtained above. The HT expansion of Ising model is as follows:

$$\mathcal{Z}^* = (\cosh(K^*))^{3N} 2^N [1 + 3N (\tanh(K^*))^4 + 18N (\tanh(K^*))^6 + \dots], \quad (\text{S19})$$

where $K^* = \beta^* J$, and $\tanh(K^*)$ is the HT expansion parameter. The series in Eqs. (S18) and (S19) are equal if $\tanh(K^*) = e^{-2K^*}$. The latter happens right at the critical temperature $T = T_c$, i.e.,

$$\tanh(K_c^*) = e^{-2K_c^*}. \quad (\text{S20})$$

This equation yields the critical temperature of the plaquette model, T_c , in terms of the critical temperature of the Ising model, T_c^* , and *vice versa*.

The HT graph or loop representation of the Ising model was earlier studied by Winter and co-workers [56] using Monte Carlo methods. The idea was to integrate out the spin variables and express the partition function in terms of closed geometrical loops. This is similar to the random cluster representation, where spin variables are integrated out and the partition function is written in terms of occupied/empty bonds; see Sec. S5. The closed loops are the HT graphs of different degrees (number of occupied bonds). Shimada et. al [57] and Kompaniets et. al [58] have also studied the fractal dimensions of these objects using conformal bootstrap and the $D = 4 - \epsilon$ expansion technique, respectively. It was found [56] that in the loop representation of the $\mathcal{O}(N = 1)$ model, the HT graphs, which are also closed loops, show a percolation transition at the Ising critical temperature T_c^* . At high T , there are only a few such small loops on the lattice, while as T decreases the loops become larger both in size and number. At $T < T_c^*$, such loops engulf the lattice, with T_c^* as their percolation temperature. We also add that in this loop representation the correlation length exponent $1/\nu$ is related to the scaling dimension Δ_ϵ of the energy operator ϵ in the 3D $\mathcal{O}(N)$ singlet sector (S). However, the exponent β/ν or the fractal dimension D_f rather pertain to the scaling dimension Δ_T of a *non-trivial* symmetric tensor operator φ_{ab} in the 3D $\mathcal{O}(N)$ tensor sector (T). See Ref. [57] for details. The latter operator is missing in the Ising Wilson CFT which is a single component theory and ideal for spin representation only. For the loop representation an appropriate theory is obtained by analytic continuation of the order parameter components N to the upper neighborhood of $N = 1$, i.e., $N \rightarrow 1^+$.

Due to the equivalence of the series (S18) and (S19), one expects that the properties of the LT expansion graphs of the gauge model, i.e., closed line loops, should be those of the Ising HT graphs.

S5. CONSTRUCTION OF FORTUIN-KASTELEYN CLUSTERS

The random cluster representation [33, 34] was introduced initially to understand the phase transition in the Potts model, where the spin variables are integrated out and the bond variables (occupied/empty) are introduced in the partition function. The distinct sets of connected occupied bonds form clusters, known as Fortuin-Kasteleyn (FK) clusters. In the Ising model, which is

a special case of Potts model, the partition function is written as follows,

$$\begin{aligned} \mathcal{Z}^* &= \sum_{\text{config.}} \prod_{\langle i,j \rangle} e^{K^*} [(1-p) + p\delta_{s_i s_j, 1}], \quad (\text{S21}) \\ &= \sum_{\text{config.}} \prod_{\langle i,j \rangle} \sum_{n_{ij}=0,1} e^{K^*} [(1-p)\delta_{n_{ij},0} + p\delta_{s_i s_j, 1}\delta_{n_{ij},1}], \end{aligned}$$

where $K^* = \beta^* J$, $p = 1 - e^{-2K^*}$, and s_i is an Ising spin sitting at each site of the cubic lattice. $n_{ij} = 0, 1$ is a bimodal random variable assigned to each bond of the configuration. The bond with $n_{ij} = 1$ is said to be occupied and it is empty if $n_{ij} = 0$. By integrating out the spin variables the partition function can be further expressed as,

$$\mathcal{Z}_{\text{FK}}^* = e^{\mathcal{N}K^*} \sum_{\{\mathcal{G}\}: \mathcal{G} \subseteq \mathcal{L}^*} p^{\mathcal{N}_{\mathcal{G}}^*} (1-p)^{\mathcal{N} - \mathcal{N}_{\mathcal{G}}^*} 2^{\mathcal{N}_{\mathcal{G}}^*}, \quad (\text{S22})$$

where $\mathcal{N}(= 3N)$ is the total number of bonds in the lattice \mathcal{L}^* , \mathcal{G} stands for the set of occupied bonds which contains $\mathcal{N}_{\mathcal{G}}^*$ number of connected components, i.e, FK clusters. $\mathcal{N}_{\mathcal{G}}^*$ and $\mathcal{N} - \mathcal{N}_{\mathcal{G}}^*$ denote the number of occupied bonds and empty bonds in such a graph, respectively. At the (inverse) temperature $\beta^* \leq \beta_c^*$ (critical one), the FK clusters percolate and their critical exponents are the same as the thermal critical exponents [34, 35].

We have seen in Sec. S4 that in the loop representation the Ising partition function \mathcal{Z}^* takes the form,

$$\mathcal{Z}_{\text{loop}}^* = (\cosh K^*)^{\mathcal{N}} 2^{\mathcal{N}} \sum_{\text{closed loops}} g_\ell^* (\tanh K^*)^\ell, \quad (\text{S23})$$

obtained via the high temperature expansion of \mathcal{Z}^* . Here, the summation is over all the closed loops with even number ℓ of links ($\ell = 0, 2, 4, \dots$) on \mathcal{L} , and g_ℓ^* is the degeneracy of loops having ℓ number of links. One can also obtain the loop configuration (S23) directly from an FK one (S22), using the Kirchhoff's conservation criterion.

Similarly, we define the random cluster representation or FK clusters for the present gauge model. Such an approach was earlier [63] exploited to obtain a cluster Monte Carlo algorithm. Likewise the Ising model, we assign a bimodal random variable $n_P = 0, 1$ to each plaquette of the lattice. Then, the partition function $\mathcal{Z} = \sum_{\text{config.}} \prod_P e^{K U_P}$ can be written as,

$$\begin{aligned} \mathcal{Z} &= \sum_{\text{config.}} \prod_P e^K [(1-q) + q\delta_{U_P, 1}], \quad (\text{S24}) \\ &= \sum_{\text{config.}} \prod_P \sum_{n_P=0,1} e^K [(1-q)\delta_{n_P,0} + q\delta_{U_P, 1}\delta_{n_P,1}], \end{aligned}$$

with $K = \beta J$ and $q \equiv 1 - e^{-2K}$. A plaquette is said to be active if $n_P = 1$ and it is empty if $n_P = 0$. Notice that in the above representation a frustrated plaquette ($U_P = -1$) is always empty, while an unfrustrated plaquette ($U_P = 1$) is empty with a probability $1-q$. An FK

cluster is formed by the neighboring “empty” plaquettes. The partition function is further written as,

$$\mathcal{Z}_{\text{FK}} = e^{\mathcal{N}K} \sum_{G \subseteq \mathcal{L}} q^{\mathcal{N}_P} (1-q)^{\mathcal{N}-\mathcal{N}_P} 2^{\mathcal{N}_G}, \quad (\text{S25})$$

where $\mathcal{N} (= 3N)$ is the total number of plaquettes in the lattice \mathcal{L} , G is the set of occupied plaquettes, and \mathcal{N}_G denotes the number of connected components which are FK clusters. \mathcal{N}_P and $\mathcal{N} - \mathcal{N}_P$ represent the number of occupied and empty plaquettes in such a graph, respectively. The loop representation (S18) of \mathcal{Z} is

$$\mathcal{Z}_{\text{loop}} = e^{\mathcal{N}K} 2^{\mathcal{N}} \sum_{\text{closed loops}} g_\ell (e^{-2K})^\ell, \quad (\text{S26})$$

which can also be obtained from the FK one (S25) by enforcing the gauge invariance (even number of plaquettes to be empty/occupied in a cube) onto FK graphs.

S6. GEOMETRIC LOOPS WITH MAXIMAL RULE AND FK CLUSTERS

Figure S5 show some plots of the percolation strength P and the susceptibility χ for the geometric loops built with the maximal connection rule and the FK clusters. These data complement the scaling plots of the same quantities in the main text. See the caption for details.

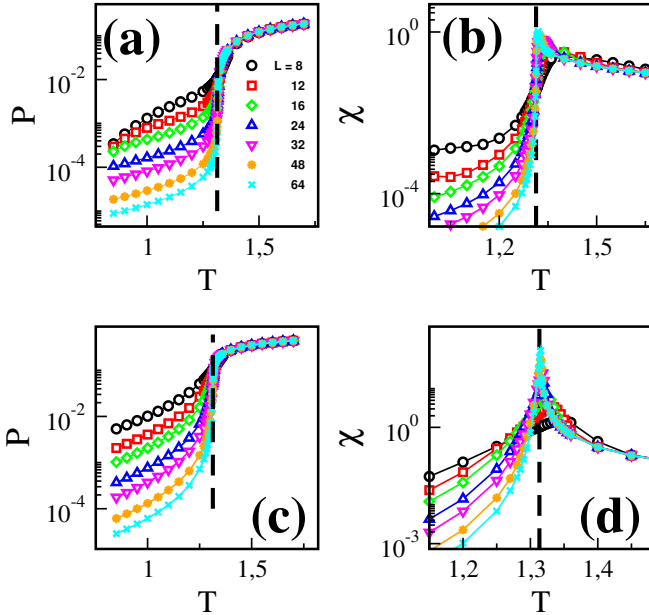


FIG. S5. (a) and (c) Percolation strength P vs T . (b) and (d) Susceptibility χ vs T . Panels (a)-(b) present data for geometric loops constructed with the maximal connection rule, while (c)-(d) do for FK clusters. Different datasets represent systems of different linear size L , see the key in (a). The vertical dotted lines are located at $T_c = 1.3133$.

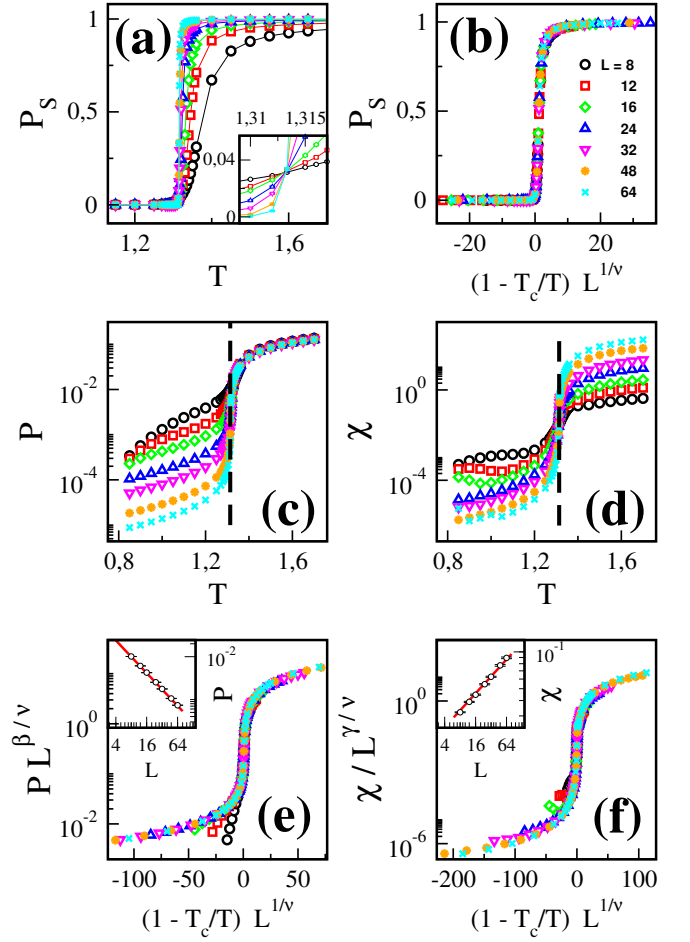


FIG. S6. Geometric line loops constructed with the stochastic connection rule. (a) Spanning probability P_S vs temperature T . (b) P_S against the scaling variable $(1 - T_c/T)L^{1/\nu}$. (c) Percolation strength P vs T . (d) Susceptibility χ vs T . (e) Rescaled plot of percolation strength, $PL^{\beta/\nu}$ vs $(1 - T_c/T)L^{1/\nu}$. (f) Rescaled plot of susceptibility, $\chi/L^{\gamma/\nu}$ vs $(1 - T_c/T)L^{1/\nu}$. Different datasets represent systems of different linear size L , see the key in (b). The inset in (a) magnifies the intersection region in the main frame. The insets in (e) and (f) display the values of P and χ at the critical temperature T_c against the system size L , with solid lines representing the laws $P \sim L^{-\beta/\nu}$ and $\chi \sim L^{\gamma/\nu}$, respectively. The vertical dashed lines in (c)-(d) are located at T_c . Different parameters are fixed to $T_c = 1.3133$, $1/\nu = 1.58$, $\beta/\nu = 1.26$, and $\gamma/\nu = 0.47$. The collapses in (b), (e), and (f) remain valid for the numerical estimates of parameters within error bars; see the text.

S7. GEOMETRIC LINE LOOPS WITH THE STOCHASTIC CONNECTION RULE

This section discusses some results for the geometric line loops constructed with the stochastic connection rule, which are complementary to those presented in the main text for the geometric line loops built with the maximal connection rule.

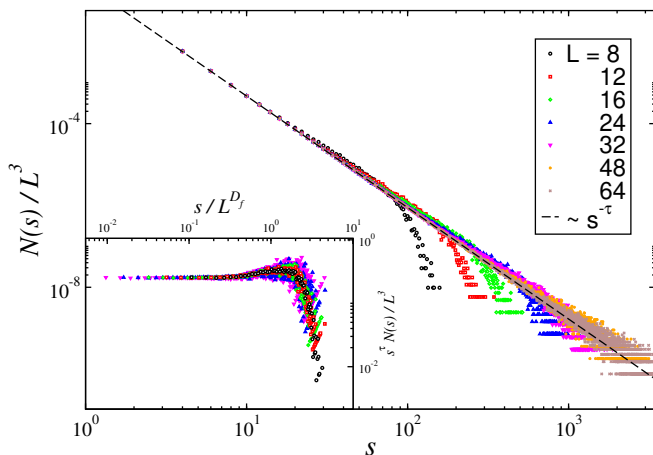


FIG. S7. Geometric line loops with the stochastic connection rule. Plots of $N(s)/L^3$ vs mass s for different system sizes L (see the key) at the critical temperature T_c . The dashed lines in both panels represent the law $N(s)/L^3 \propto s^{-\tau}$, with $\tau = 2.71$. The insets plot the scaling variable $s^\tau N(s)/L^3$ against s/L^{D_f} for the data in the corresponding main frames. Herein, τ and D_f are fixed to $\tau = 2.71$ and $D_f = 1.74$.

In Fig. S6, we plot several quantities that characterize the percolation transition. In (a) we plot the spanning probability P_S against temperature for different systems of linear sizes L . Similar to what we found with the maximal rule, P_S approaches zero for low T , while it tends to unity for high T . The value of the percolation temperature T_p obtained from the intersection point of the datasets for different L (see inset) is $T_p \simeq 1.3132(2)$, which is in excellent agreement with the theoretical critical temperature T_c as well as with the one obtained from the maximal connection rule. In (b) P_S is plotted against the scaling variable $(1 - T_c/T)L^{1/\nu}$ to verify the scaling relation (S9). Here, we fix $T_p = T_c$ as obtained in panel (a) and we treat the exponent ν as a free parameter. An excellent scaling collapse is observed for $1/\nu \simeq 1.60(3)$, which also matches quite well with $1/\nu \sim 1.59$ for the 3DIM within numerical precision.

In panels (c) and (d) of Fig. S6, the percolation probability P and susceptibility χ are plotted against T , respectively. While the behavior of P is akin to the one of the loops built with the maximal connection rule, χ shows a strange behavior for $T \geq T_c$; see Sec. S6 for comparison with the results for the maximal connection rule. Generally, a peak in χ is observed around $T_c(L)$, which approaches the theoretical value of T_c with L (i.e., in the thermodynamic limit). Beyond $T > T_c(L)$ the χ continuously decreases with T . However, in the present panel (d) χ seems to increase. The reason for this unexpected behavior is the stochastic connection method of geometric loops [30, 31]. In this method, whenever a knot in the line loops is encountered, a dice (random variable between 0 and 1) is thrown to resolve it such that the loops do not cross each other. Therefore, the length of the resulting loops is shorter than the length of

those obtained from the maximal connection methods. Especially, above T_c as the number of frustrated plaquettes increases with T , the number of loops obtained from the stochastic rule also increases. Therefore, the susceptibility χ (variance of mass fraction m of the largest loop in the system, see Eq. (S6)), also increases with T . The latter does not happen for the maximal connection rule as only a few loops evade the whole system and only very small other loops complete the picture.

In panels (e) and (f) of the same figure, the scaling functions [Eqs. (S7)-(S8)] of P and χ are checked, and the power-law behavior of these quantities at T_c is verified in the respective insets. Both main panels show excellent data collapse when using $T_p = T_c$ and the value of $1/\nu$ as obtained above, and treating the exponents β/ν and γ/ν as free parameters. The values of these exponents so obtained agree with the power law behavior of the quantities $P \sim L^{-\beta/\nu}$ and $\chi \sim L^{\gamma/\nu}$ in the insets, respectively [$\beta/\nu \simeq 1.269(7)$ and $\gamma/\nu \simeq 0.478(16)$]. Interestingly, the scaling collapse of χ remains good in the full range of T , despite the fact that the behavior of χ is unusual for $T > T_c$.

Finally, akin to the maximal rule, for the stochastic rule the values of exponents $1/\nu$, β/ν and γ/ν are the same as those of HT graphs in 3DIM within numerical precision.

In Fig. S7, the number density of loops, built with the stochastic rule, with mass s at $T = T_c$ is plotted. The power law behavior (S10) is clearly obeyed in the plot, with the exponent $\tau \sim 2.72(1)$ which is in good agreement with the one found with the maximal rule; see main text. In the inset the scaling relation (S30) is also verified.

S8. BINDER CUMULANT OF THE PERCOLATION ORDER PARAMETER

The Binder cumulant U_4 is an important quantity to characterize the nature of geometric as well as thermal phase transitions [60]. In the present system, it can be calculated from the distribution $P_{\text{dist}}(m)$ of the mass fraction m of largest object as,

$$U_4 = 1 - \frac{\langle m^4 \rangle}{3\langle m^2 \rangle^2}, \quad (\text{S27})$$

where the symbol $\langle(\dots)\rangle$ represents the average over independent equilibrium configurations. The ratio $\langle m^4 \rangle / \langle m^2 \rangle^2$ represents the kurtosis of the distribution $P_{\text{dist}}(m)$. In the percolation phase $T > T_p$, both $\langle m^4 \rangle$ and $\langle m^2 \rangle^2$ are equal, i.e., $U_4 = 2/3$ for $T \gg T_p$. However, at low T , the geometrical objects are scarce as very less number of plaquettes are frustrated (no frustrated plaquette at $T = 0$). As a result, the distribution of m becomes skinny around the mean with long tails.

In a continuous phase transition, U_4 has a scaling form analogous to the one of the spanning probability (S9). It

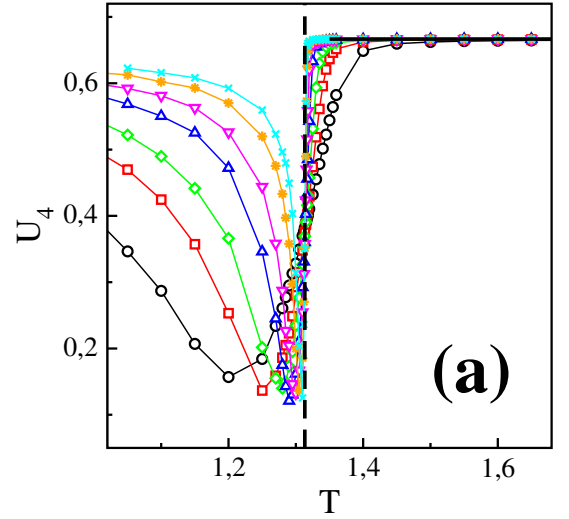
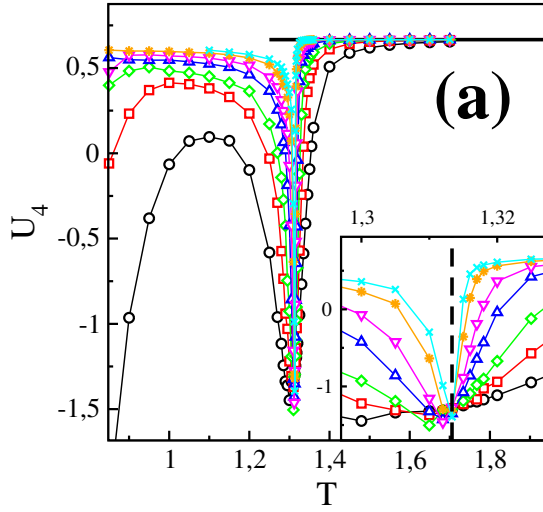


FIG. S8. (a) Binder cumulant U_4 vs temperature T for line loops formed with the maximal connection rule. The horizontal line represents the large- T behavior, i.e. $U_4 = 2/3$. The inset in (a) magnifies the dip and intersection region, with the vertical dashed line locating the critical temperature T_c . (b) Scaling plot of U_4 for the data in (a), having fixed $T_p = T_c$ and $1/\nu = 1.58$. The inset in (b) magnifies the data collapse of the main frame around the dip. Different datasets represent the systems of different linear size L ; see the key in (b).

reads

$$U_4 = f_U \left[\left(1 - \frac{T_p}{T} \right) L^{1/\nu} \right]. \quad (\text{S28})$$

At $T = T_p$, U_4 takes a universal value independent of system size L , $U_4 = f_U[0]$, i.e., the datasets belonging to the different system size should intersect each other.

In Fig. S8, the behavior of U_4 for the geometric line loops constructed with the maximal connection rule is explored. In panel (a), U_4 is plotted against temperature T for different system sizes L . The value of T_p is obtained from the common intersection of different

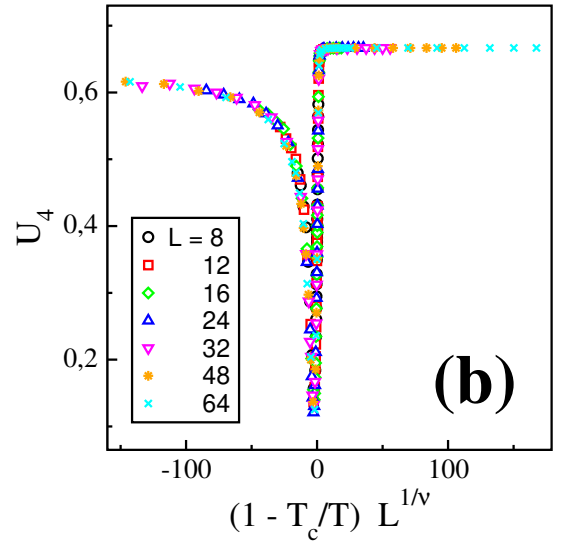


FIG. S9. Plots similar to Fig. S8, but for FK graphs. In (b), the parameters are fixed to $T_p = T_c$ and $1/\nu = 1.58$.

datasets, $T_p \simeq 1.3135(3)$, which is in excellent agreement with T_c . For $T > T_p$, U_4 approaches a limiting value $2/3$ independently of L , while at low T the value of U_4 decreases on lowering L and even becomes negative for small L and weak T . This fact is in contradiction with what is expected in conventional continuous phase transitions, where U_4 approaches zero due to Gaussianity of the order parameter (kurtosis equals 3). When magnifying the data of this panel in the inset, it is found that the different datasets intersect at a common point, which is indistinguishable from T_c . This L -independent behavior of U_4 at T_c is a signature of continuous transition. In addition, for each L a strange dip in U_4 is also observed near (but below) T_c . If this dip were to increase rapidly with L , one should conclude that the transition is of first order. However, the inset also shows that the dip does not change a lot with the system size. In the literature [61, 62], such a behavior was predicted

due to anomalies in the order parameter distribution (see Fig. S10) near T_c and the transition was referred to as *pseudo first order transition*. A more quantitation understanding is developed below.

In the panel (b) of Fig. S8, the scaling relation (S28) is tested for the data in (a) while fixing $T_p = T_c$ and treating ν as a free parameter. The best scaling collapse for datasets belonging to different L is obtained for $1/\nu \simeq 1.571(18)$. To judge the quality of the collapse, data of the main frame are magnified around the dip and common intersection in the inset, which confirms the validity of the relation (S28). Since both dip and common intersection are described by the same scaling relation (S28), it can be concluded that the observed dip is also a universal feature of the fixed point at T_c . Therefore, the percolation transition in line loops is of continuous topological nature. A similar picture is obtained for line loops constructed from the stochastic rule. Notice that the values of T_c and $1/\nu$ obtained above are in good match with the ones extracted from the spanning probability P_S in the main text.

In Fig. S9, the same analysis is repeated for the FK graphs. The behavior is analogous to the one of the line loops (a common intersection at $T_p = T_c$ and slowly varying dip right below T_c for different L), though the value of U_4 remains nonzero at low T . Furthermore, a perfect agreement is obtained for the scaling relation (S28) in the whole range of T . This analysis gives $T_p \simeq 1.3139(6)$ and $1/\nu \simeq 1.575(15)$, which are in good agreement with those obtained from P_S in the main text.

Finally, the percolation transition in the FK graphs is also of continuous topological nature with characteristics of a pseudo first order transition.

Figure S10 shows the probability distribution $P_{\text{dist}}(m)$ for (a) line loops and (b) FK graphs, above, below, and at T_c . See the caption for details. At $T \gtrsim T_c$ the behavior of $P_{\text{dist}}(m)$ is similar to what is expected in a conventional continuous phase transition [36]. However, as the temperature is lowered below T_c it shows significant differences. $P_{\text{dist}}(m)$ is not Gaussian and produces a value of kurtosis different from 3 (see the insets). Therefore, U_4 no longer approaches zero in the disordered phase. The dip in U_4 below T_c can be related to such anomalies in $P_{\text{dist}}(m)$ [61, 62]. Notice that the different behavior of $P_{\text{dist}}(m)$ at T_c in (a) and (b) is due to the localization error in T_c .

S9. FRACTAL CHARACTER OF GEOMETRIC OBJECTS AT THE CRITICAL POINT

This section explores the fractal characteristics of the different geometric objects and their substructures at the percolation threshold, which coincides with the thermodynamic critical temperature T_c (see the main text). For this purpose, we calculate the fractal dimension D_f of these objects and the backbone exponent D_b to be defined below.

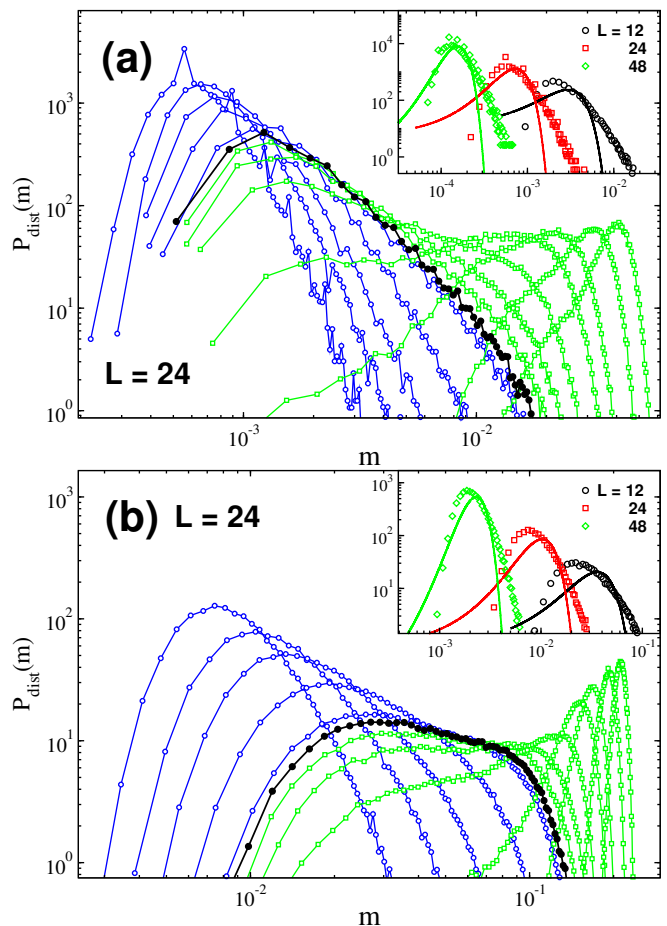


FIG. S10. Probability distribution $P_{\text{dist}}(m)$ vs mass fraction m for (a) line loops with maximal connection, and (b) FK graphs, for temperatures below (denoted by circle), above (denoted by square), and at the T_c (filled circle). The temperature increases as the maximum in $P_{\text{dist}}(m)$ shifts from left to right. The linear size of the system is fixed to $L = 24$. Insets in (a) and (b) show the probability distribution $P_{\text{dist}}(m)$ for $T = 1.27$ and different system sizes (see the key). The curves in solid plotted above the different datasets, represent the Gaussian distribution with mean and variance determined from those datasets.

For convenience of the reader, we recall that a percolating cluster consists of many fractal substructures. In particular, a backbone is subset of those *special* constituents (sites/bonds) which would carry the electric current if a voltage difference is set up across the opposite edges of the percolating cluster. The exponent D_b is associated with this backbone structure and it is useful to distinguish different fractal objects with similar value of D_f (see Refs. [41, 43] for a detailed discussion).

Here, we exploit a computationally efficient method to estimate D_b . In the present model, the loops/clusters are constructed by the lines which thread the neighboring frustrated plaquettes of the lattice. Therefore, a line passing through two neighboring plaquettes (belonging to same cube) serves as a “bond” between them. We

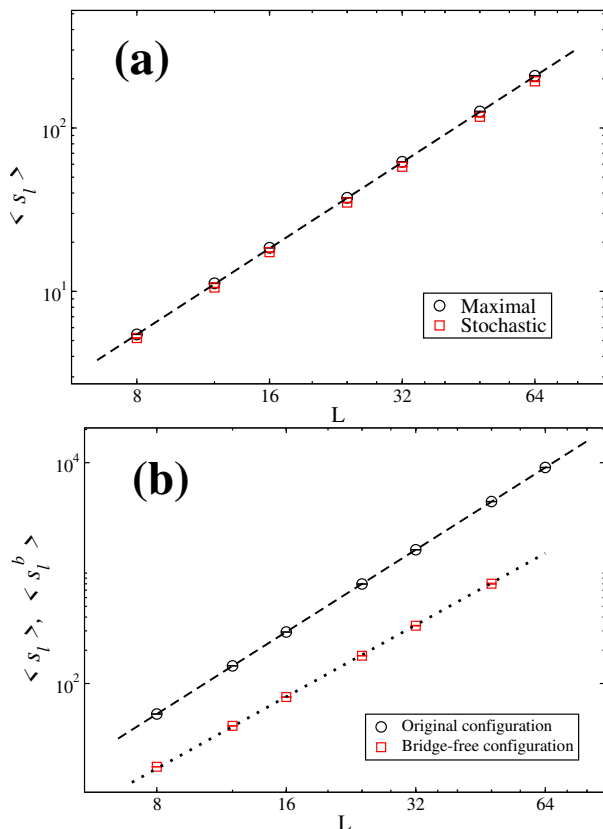


FIG. S11. (a) Plot of $\langle s_l \rangle$ vs L for closed line loops formed with different connection methods (see the key). The dashed line represents the best power-law fit to the law $\langle s_l \rangle \sim L^{D_f}$, with $D_f \simeq 1.74$. (b) Plot of $\langle s_l \rangle$ (circle) and $\langle s_l^b \rangle$ (square) against L for Fortuin-Kasteleyn (FK) clusters. The dashed and dotted lines represent the best fit to $\langle s_l \rangle \sim L^{D_f}$ and $\langle s_l^b \rangle \sim L^{D_b}$, with $D_f = 2.48$ and $D_b = 2.16$, respectively. The error bars in both panels are smaller than the symbol sizes.

classify such bonds into two categories, *bridge* bonds and *non-bridge* bonds. A bridge bond is such that, when removed, the cluster breaks up into two separate clusters. Otherwise, the bond is called non-bridge. In the next step, all the bridge bonds are removed from an original plaquette configuration. The configuration so obtained does not have dangling ends excluding the small to large sized blobs. The average mass $\langle s_l^b \rangle$ of the largest blob gives the backbone exponent D_b as,

$$\langle s_l^b \rangle \sim L^{D_b}. \quad (\text{S29})$$

We remind that the line loops constructed from any connection method cannot have dangling ends. Therefore, their backbone exponent D_b is equivalent to their fractal dimension D_f . This is not the case for the lines built from the FK clusters and for them D_b can be different from D_f . Moreover, D_b for the FK clusters needs not be the same as D_f for the line ones.

In Fig. S11(a), the average mass $\langle s_l \rangle$ of the largest closed loops is plotted against the system size L for

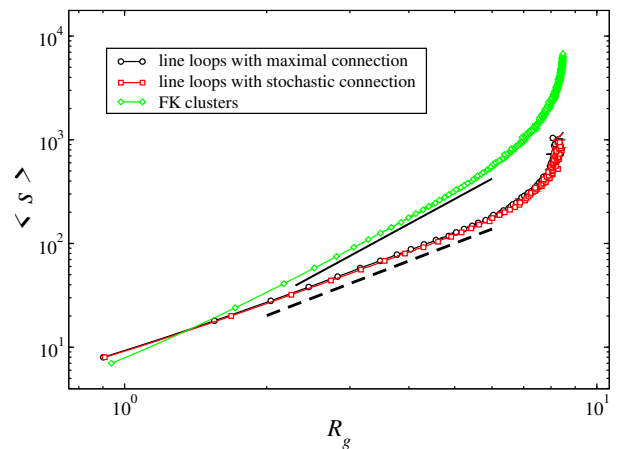


FIG. S12. Average mass $\langle s \rangle$ against the radius of gyration R_g , for a pure gauge system of linear size $L = 24$. Different datasets represent different geometric objects (see the key). The solid and dashed lines denote the law $\langle s \rangle \sim R_g^{D_f}$, with fractal dimensions $D_f = 1.74$ and $D_f = 2.48$, respectively.

both connection methods, maximal and stochastic. This quantity shows a power-law growth on the log-log scale of the figure, as described in Eq. (S13). We obtain $D_f \simeq 1.738(8)$ irrespective of the connection method. This value of D_f is in excellent agreement with that of the HT expansion graphs in the 3D Ising model [56–58] (see the discussion in the above section).

In Fig. S11(b), $\langle s_l \rangle$ and $\langle s_l^b \rangle$ are calculated for the FK clusters, which are extracted from the original and bridge-free configurations, respectively. From the best power-law fits to different datasets in Fig. S11(b), we obtain $D_f \simeq 2.481(6)$ and $D_b \simeq 2.159(8)$, which are in agreement with the recent numerical estimates for FK clusters in 3D Ising model [36].

For a consistency check, we also calculate the fractal dimension D_f from the standard box counting approach, i.e., using Eq. (S15). We plot the average mass $\langle s \rangle$ of the different geometric objects (represented by different datasets) against their radius of gyration R_g in Fig. S12, for a system of linear size $L = 24$. On the scales larger than the lattice spacing ($R_g > 1$), a quite good agreement is observed with the above estimates of D_f . Notice that the bend in datasets at large R_g is due to finite size effects and goes away with increase in system size.

S10. STATISTICS OF LINE LOOPS AT DIFFERENT TEMPERATURES

Equation (S10) reveals that at the percolation temperature T_p (which coincides with the critical temperature T_c for the line loops; see the main text) the number density $N(s)$ of loops with length s falls in a power law fashion, $N(s)/L^3 \propto s^{-\tau}$, as the tension vanishes, $\epsilon = 0$, at $T = T_p$. This can be expressed in terms of a finite size

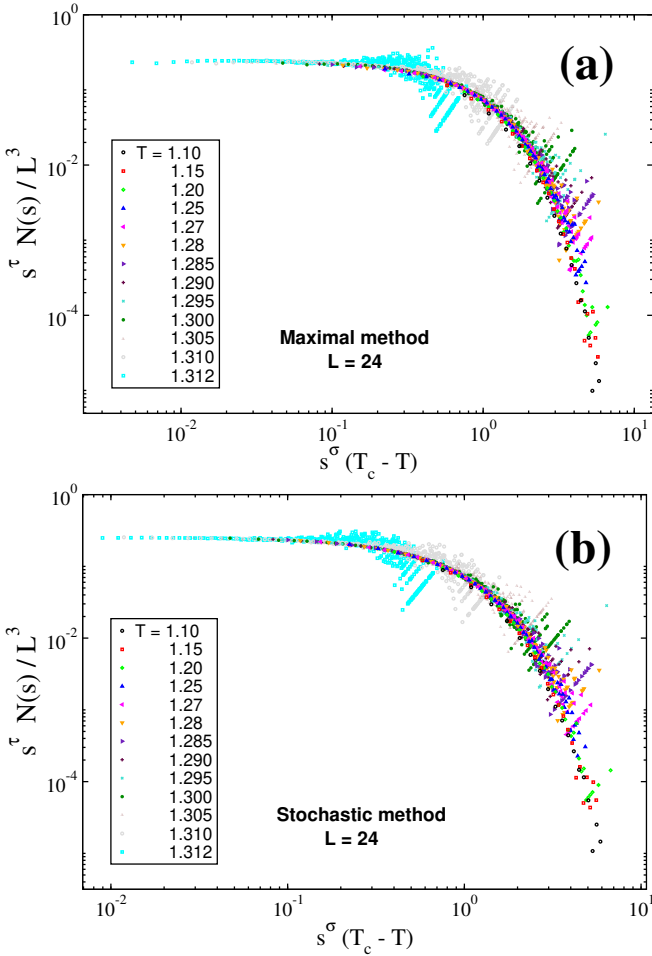


FIG. S13. Scaling plots of $s^\tau N(s)/L^3$ vs $s^\sigma(T_c - T)$ for a system of linear size $L = 24$ at different temperatures below T_c (see the key): (a) maximal and (b) stochastic connection of closed line loops. Herein, τ is fixed to $\tau = 2.71$.

scaling function as,

$$N(s)/L^3 = s^{-\tau} G(s/L^{D_f}), \quad (\text{S30})$$

where D_f is the fractal dimension. In the main text and Sec. S7 the above laws are justified for maximal and stochastic connection methods of the loops, respectively. The law $N(s)/L^3 \propto s^{-\tau}$ is also confirmed with exponent $\tau \simeq 2.715(15)$ for the line loops, irrespective of the connection rule used.

We recall that for temperatures below T_c , Eq. (S10) remains valid but with a nonzero tension ϵ . We reformulate the scaling law (S10) as,

$$N(s)/L^3 \simeq s^{-\tau} f_N(s^\sigma |T - T_c|), \quad (\text{S31})$$

where f_N is a scaling function. The above relation allows us to extract the value of the exponent σ and cross check with the obtained value of the exponent ν in the main text, as $\sigma = 1/(D_f \nu)$. In Figs. S13(a) and (b), the above law is checked for maximal and stochastic connections, respectively, where the size of the system is $L = 24$ and

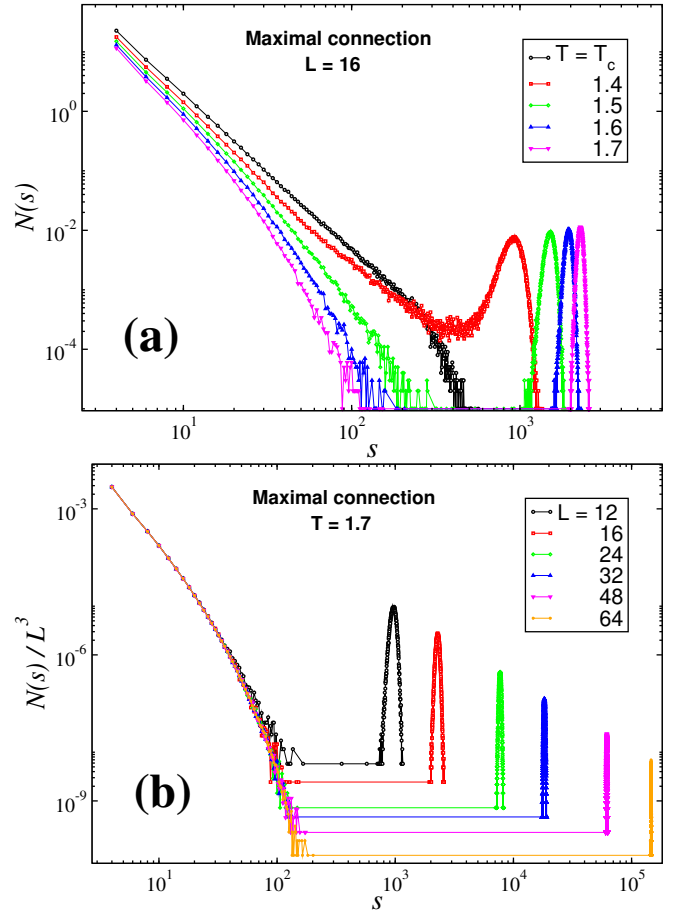


FIG. S14. Closed loops with maximal connection. (a) Plot of $N(s)$ vs s for a system of linear size $L = 16$ at different temperatures above and at T_c (see the key). (b) Plot of $N(s)/L^3$ vs s for different system sizes L (see the key) and temperature $T = 1.7$.

different datasets correspond to temperatures below T_c . Here, the value of τ is fixed to $\tau \simeq 2.71$ (as obtained above), and the value of the exponent σ is chosen so as to enable a good scaling collapse for different datasets. We obtain

$$\sigma \simeq 0.91(1) \quad (\text{S32})$$

in both figures. (The large s deviation from the collapse is a finite size effect, as the scaling law (S31) is valid for the small loops only.)

Now we finally discuss the statistics of line loops at high temperatures ($T \gg T_c$), for which some generic predictions for $N(s)$ are available from the so-called fully-packed loop models. The equilibrium configuration at high temperatures is filled with system spanning line defects. If the configuration is so packed that two line defects enter and exit each elementary cube, the number density $N(s)$ of geometrical loops of length s behaves

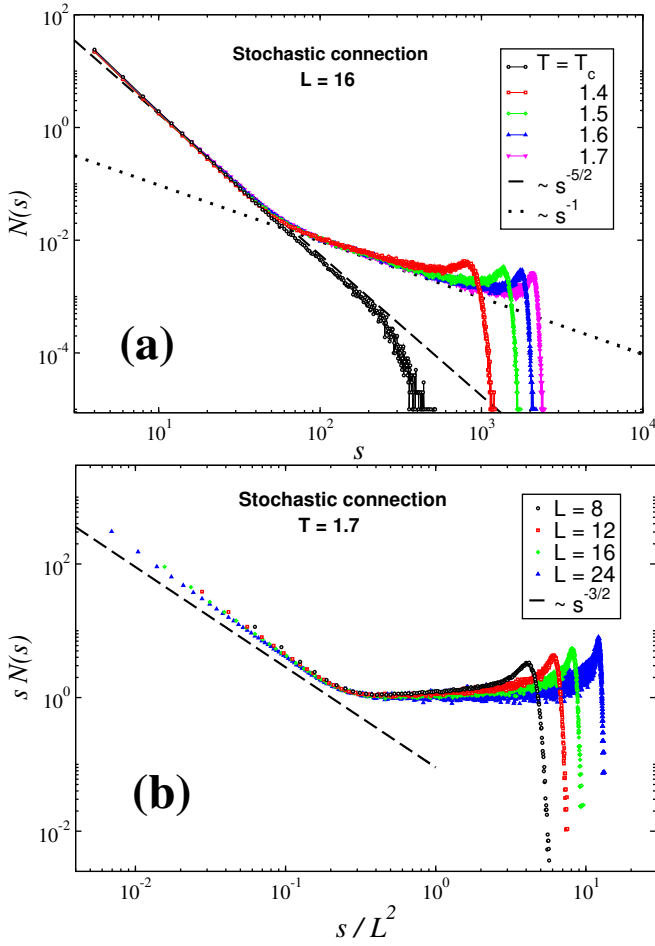


FIG. S15. Closed loops with stochastic connection. (a) Plot of $N(s)$ vs s for a system of linear size $L = 16$ at different temperatures above and at T_c (see the key). The dashed and dotted lines represent the laws $N(s) \sim s^{-5/2}$ and $N(s) \sim s^{-1}$, respectively. (b) Plot of $sN(s)$ vs s/L^2 for different system sizes L (see the key) and temperature $T = 1.7$. The dashed line represents the power law $y(x) \sim x^{-3/2}$.

as [65],

$$N(s)/L^3 \simeq \begin{cases} s^{-5/2}, & s \ll L^2, \\ s^{-1}L^{-3}, & s \gg L^2. \end{cases} \quad (\text{S33})$$

The small scale regime $s \ll L^2$ corresponds to the result for a Gaussian random walk [65], while the large scale regime supports the fully-packed loop model prediction [65].

Here, we test the predictions in Eq. (S33) for the line loops in the present model formed by different connection methods. In Fig. S14(a), the quantity $N(s)$ is plotted against s for the maximal connection rule, for a system with linear size $L = 16$. In contrast to the prediction in Eq. (S33), $N(s)$ indicates an exponential fall at small s , while only a peak is obtained at large s . The position of the peak increases with the temperature T above T_c . In Fig. S14(b), the behavior of the quantity $N(s)$ is tested

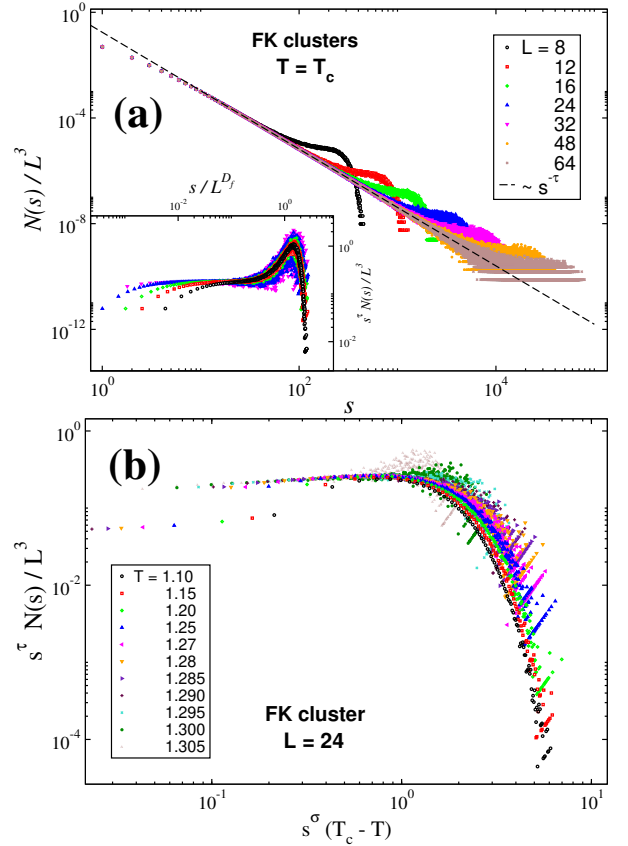


FIG. S16. FK clusters: (a) Plot of $N(s)/L^3$ vs s for different system sizes L (see the key) at the critical temperature T_c . The dashed line represents the law $N(s)/L^3 \propto s^{-\tau}$, with $\tau = 2.21$. In the inset, the scaling variable $s^\tau N(s)/L^3$ is plotted against s/L^{D_f} for the data in main frame, with τ and D_f fixed to $\tau = 2.21$ and $D_f = 2.48$. (b) Scaling plot of $s^\tau N(s)/L^3$ vs $s^\sigma (T_c - T)$ for a system of linear size $L = 24$ at different temperatures below T_c (see the key), with $\tau = 2.21$.

for different system sizes while fixing temperature to a higher $T = 1.7$. With increase in L , the regime of initial exponent fall increases. Apart from that, the peak position is also shifted to large s . This actually demonstrates that due to the maximal connection criterion, the system at high temperatures is evaded by a very large loop (which wraps around the periodic boundaries several times). Other remaining loops are very small (both in size and number) and therefore, they cannot produce the law (S33).

Instead, the predictions in Eq. (S33) are nicely verified by the line loops constructed with the stochastic method, as shown in Fig. S15. In Fig. S15(a), $N(s)$ is plotted against s for $L = 16$. The data in this figure clearly show agreement with the law (S33): $N(s) \sim s^{-5/2}$ for small s and $N(s) \sim s^{-1}$ for large s . The same behavior is also found for other system sizes (not shown here for brevity). To confirm the two power laws in Eq. (S33) more explicitly, the quantity $sN(s)$ is plotted against s/L^2 for different system sizes and $T = 1.7$ in Fig. S15(b). A power

law decay $s^{-3/2}$ at $s \ll L^2$ and a constant behavior at $s \gg L^2$ is observed in such kind of plot, which confirms the validity of (S33).

The results in this section are quantitatively similar to the ones in Refs. [30, 31].

S11. NUMBER DENSITY OF FK CLUSTERS

To extract the critical exponents τ and σ for the FK clusters, one can borrow the analysis presented above for the line loops, i.e., to exploit the finite-size scaling function (S30) and law (S31) for the number density $N(s)$. We remind that similarly to the line loops, the percolation temperature T_p of the FK clusters also coincides with the critical temperature T_c ; see the main text.

In the main frame of Fig. S16(a), the normalized number density $N(s)/L^3$ of the FK clusters is plotted against their mass s for different system sizes L at the critical temperature $T = T_c$. As expected from Eq. (S10), this

quantity decays algebraically at T_c , $N(s)/L^3 \sim s^{-\tau}$, with

$$\tau \simeq 2.207(5) . \quad (\text{S34})$$

This value of τ gives $D_f \simeq 2.48$, which is in agreement with our direct probe of $D_f[\simeq 2.481(6)]$ from $\langle s_l \rangle$. In the inset of Fig. S16(a), the validity of the function (S30) is tested when fixing $\tau \simeq 2.21$ and $D_f \simeq 2.48$. The deviation from the scaling collapse at small s (on the order of the lattice spacing) is obvious as the function (S30) is valid only for the fractal clusters.

In Fig. S16(b), the scaling law (S31) is tested by plotting the quantity $s^\tau N(s)/L^3$ against the variable $s^\sigma(T_c - T)$ for the FK clusters in a system of linear size $L = 24$. We fixed τ to $\tau \simeq 2.21$, and the exponent σ is estimated by enabling the good scaling collapse of the different datasets. Notice that the function f_N in Eq. (S31) accounts for how the number density $N(s)$ of cluster size s changes near T_c , but it does not consider the role of the system size L . Therefore, finite size corrections are expected in this law. We find

$$\sigma \simeq 0.64(1) , \quad (\text{S35})$$

which is also in agreement with the definition $\sigma = 1/(D_f\nu)$.